

Heavy axion-like particles and core-collapse supernovae: constraints and impact on the explosion mechanism

Giuseppe Lucente,^a Pierluca Carenza,^{a,b} Tobias Fischer,^c Maurizio Giannotti,^d Alessandro Mirizzi^{a,b}

^aDipartimento Interateneo di Fisica “Michelangelo Merlin”, Via Amendola 173, 70126 Bari, Italy

^bIstituto Nazionale di Fisica Nucleare - Sezione di Bari, Via Orabona 4, 70126 Bari, Italy

^cInstitute for Theoretical Physics, University of Wrocław, Pl. M. Borna 9, 50-204 Wrocław, Poland

^dPhysical Sciences, Barry University, 11300 NE 2nd Ave., Miami Shores, FL 33161, USA

E-mail: g.lucente5@studenti.uniba.it, pierluca.carenza@ba.infn.it,
tobias.fischer@ift.uni.wroc.pl, MGiannotti@barry.edu,
alessandro.mirizzi@ba.infn.it

Abstract. Heavy axion-like particles (ALPs), with masses $m_a \gtrsim 100$ keV, coupled with photons, would be copiously produced in a supernova (SN) core via Primakoff process and photon coalescence. Using a state-of-the-art SN model, we revisit the energy-loss SN 1987A bounds on axion-photon coupling. Moreover, we point out that heavy ALPs with masses $m_a \gtrsim 100$ MeV and axion-photon coupling $g_{a\gamma} \gtrsim 4 \times 10^{-9} \text{ GeV}^{-1}$ would decay into photons behind the shock-wave producing a possible enhancement in the energy deposition that would boost the SN shock revival.

Contents

1	Introduction	1
2	Input of our calculation	2
2.1	SN reference model	2
2.2	Effective proton mass and chemical potential	3
2.3	Neutrino opacity	5
2.4	The characteristic radii	6
3	ALP emissivity in a supernova	8
3.1	Primakoff process	8
3.2	Photon coalescence	10
4	SN 1987A ALP bounds	11
4.1	Free-streaming regime	11
4.1.1	Energy-loss argument	11
4.1.2	Gravitational trapping	12
4.2	Trapping regime	13
4.3	Modified luminosity criterion	16
5	Shock revival and ALP energy deposition	19
6	Conclusions	24

1 Introduction

Axion-like-particles (ALPs) with masses m_a in the keV-MeV range emerge in different extension of the Standard Model, as Pseudo-Goldstone bosons of some broken global symmetry (see, e.g. Sec. 6.7 of Ref. [1] for a recent review). Besides QCD axions, heavy ALPs emerge in compactification scenarios of string theory [2–4], or in the context of “relaxion” models [5]. Heavy ALPs have also recently received considerable attention in the context of Dark Matter model-building. Indeed, they may act as mediators for the interactions between the Dark Sector and Standard Model (SM) allowing to reproduce the correct Dark Matter relic abundance via thermal freeze-out [6, 7]. ALPs with masses below the MeV scale can have a wide range of implications for cosmology and astrophysics (see [8] for a review), affecting for example the Big Bang Nucleosynthesis (BBN), the Cosmic Microwave Background (CMB) [9–11] and the evolution of stars [12]. Colliders and beam-dump experiments are also capable to explore this mass range, indeed reaching the $m_a \sim \mathcal{O}(\text{GeV})$ frontier, which is not covered by any astrophysical or cosmological considerations [8, 13, 14].

Core-collapse supernovae (SNe) represent a valuable cosmic laboratory to probe ALPs [15–17]. In this minimal scenario, in which ALPs couple only with photons with an effective two-photons vertex $g_{a\gamma}$, their dominant emission process in SNe is constituted by the Primakoff process on free protons, $\gamma + p \rightarrow p + a$, i.e. the conversion of a photon into an ALP in the electric field of protons in the stellar matter. Moreover, in a medium of sufficiently high density, two photons can annihilate producing an axion, in the so called “photon coalescence” or “inverse decay process”. This effect has a kinematic threshold, vanishing for

$m_a < 2\omega_{\text{pl}}$, where the plasma frequency ω_{pl} is the “effective photon mass”. This process, typically neglected in previous studies, in a SN core starts to be important for $m_a \gtrsim 10$ MeV. ALP emission from SNe has been used to obtain constraints on the photon-ALP coupling $g_{a\gamma}$ from the SN 1987A neutrino burst [8, 18, 19]. Indeed for values of $g_{a\gamma} \gtrsim 10^{-9} \text{ GeV}^{-1}$, ALPs would have contributed to an excessive energy-loss in the SN core, shortening the observed neutrino burst. The couplings $g_{a\gamma} \lesssim 10^{-5} \text{ GeV}^{-1}$ have also been excluded. Indeed, in this range ALPs would be trapped in a SN core, contributing to an excessive energy-transfer. Furthermore, in [20, 21] it has been shown that for coupling $g_{a\gamma} < 10^{-9} \text{ GeV}^{-1}$, in the mass range $m_a \in [1, 100] \text{ MeV}$ a further constrain can be obtained from the non-observation of a gamma-ray flux from decaying ALPs, in coincidence with SN 1987A neutrino burst.

The goal of our paper is to take a fresh look to the SN 1987A energy-loss argument on heavy ALPs, characterizing the ALP emissivity using state-of-the-art SN simulations. Moreover, we will examine the possible impact of ALPs on the SN explosion mechanism, in scenarios in which these particles decay into photons behind the SN shock-wave, helping its revitalization. The plan of our work is as follows. In Sec. 2 we present our SN reference model. In Sec. 3 we characterize the ALP emissivity from Primakoff and photon coalescence processes. Sec. 4 presents our update of the bounds on heavy ALPs from SN 1987A. In Sec. 5 we discuss the possible impact of decaying ALPs behind the shock-wave on the SN explosion mechanism. Finally, in Sec. 6 we summarize our results and we conclude.

2 Input of our calculation

2.1 SN reference model

In this work, we consider as SN reference model **AGILE-BOLTZTRAN**, which is based on spherically symmetric neutrino-radiation hydrodynamics with accurate three-flavor Boltzmann neutrino transport [22, 23], including a complete set of standard weak interactions (see Table 1 in Ref. [24]). The SN simulations are launched from the $18 M_{\odot}$ progenitor from the stellar evolution calculations of Ref. [25].

Neutrino-driven explosions cannot be obtained in spherically symmetric simulations, except for low-mass progenitor stars with masses of $M \simeq 8 - 9 M_{\odot}$ (featuring O-Ne-Mg cores [26, 27] and being associated with electron-capture SN [28]). Thus enhanced neutrino heating rates have been applied here in order to trigger the SN explosion onset at a post-bounce time $t_{\text{pb}} \approx 220 \text{ ms}$, following the procedure developed in Ref. [29]. Once the explosion proceeds, the standard rates are restored. This artificial tool does not affect our results since the ALP production becomes relevant on a timescale on the order of one second after the supernova explosion has been launched. As a matter of fact, the supernova evolution at $t \gtrsim \mathcal{O}(1 \text{ s})$ is moderately independent from the details of the explosion mechanism and it can be well simulated in a spherical symmetry since multidimensional phenomena play a minor role for determining the structure at the proto-neutron star interior where our focus will be on the high-density and high-temperature domain.

For the calculation of the ALP emissivity, we are interested in the deepest SN regions. In particular, in Fig. 1 we show in the plane of radial coordinate r vs post-bounce time t_{pb} the isocontours of temperature T (left panel) and density ρ (right panel). Due to the proto-neutron star contraction, the core density monotonically increases till it exceeds the nuclear saturation density ($\rho_{\text{sat}} \approx 2.5 \times 10^{14} \text{ g cm}^{-3}$) for $r \lesssim 10 \text{ km}$. On the other hand, at early times after the core bounce ($t_{\text{pb}} \sim 1 - 3 \text{ s}$) the highest temperatures [$T \sim \mathcal{O}(40 \text{ MeV})$] are

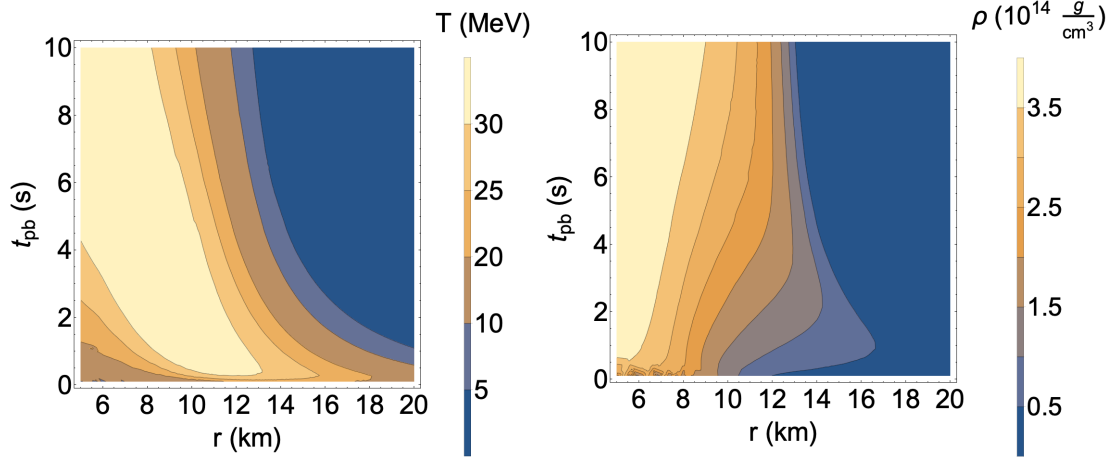


Figure 1. Isocontours of temperature T (left panel) and of the matter density ρ (right panel) in the plane r – t_{pb} .

reached at $r \approx 6 - 12$ km. At late times ($t_{\text{pb}} \sim 10$ s), the temperature is the highest at the centre and decreases with the radius.

2.2 Effective proton mass and chemical potential

In order to evaluate the ALP production rate, in particular the axion emission due to the Primakoff process, we have to consider two nuclear matter aspects, accounted in SN simulations: the reduction of the nuclear masses due to medium effects and the possible degeneracy of protons. Both phenomena depend on the nuclear equation of state for which the relativistic mean field model of Ref. [30] is employed here (further details can be found in Ref. [31, 32]). In particular, in the hot and dense supernova matter protons are in chemical and thermal equilibrium and obey the Fermi-Dirac statistics with the following distribution function f_p ,

$$f_p(p; \{\mu_p, T\}) = [\exp\{\beta(E(p) - \mu_p^*)\} + 1]^{-1}, \quad (2.1)$$

with inverse temperature $\beta = 1/T$ and effective chemical potential μ_p^* . Commonly used modern nuclear equations of state for supernova studies consider the strongly interacting nucleons at the mean field level [30, 31], which are based on the single-particle self energy, Σ , that can be separated into scalar (S) and the vector parts (V). This leads to the nucleon energy dispersion relation, $E(p) = \sqrt{p^2 + m_p^*}$ with the proton effective mass, $m_p^* = m_p - \Sigma_p^S$, and the definition of the effective chemical potential as follows, $\mu_p^* = \mu_p - \Sigma_p^V$, related with the proton thermodynamic chemical potential, μ_p . Note that we distinguish proton and neutron self energies here, in accordance with Ref. [31]. The difference between neutron and proton self energies is related with the nuclear symmetry energy, which has a strong density dependence [33]. In the left panel of Fig. 2 the isocontours of the ratio m_p^*/m_p in the r – t_{pb} plane are shown. We observe that at $r < 10$ km the effective proton mass is reduced by 50% with respect to its vacuum value. Indeed, the effective mass reduces steeply with increasing density above the nuclear saturation density, due to the strong density dependence of the scalar interactions in relativistic mean-field nuclear equations of state.

Note further that in our calculations of the axion emission rate, we assume non-relativistic protons and the argument in the exponent of the Fermi-Dirac distribution function becomes

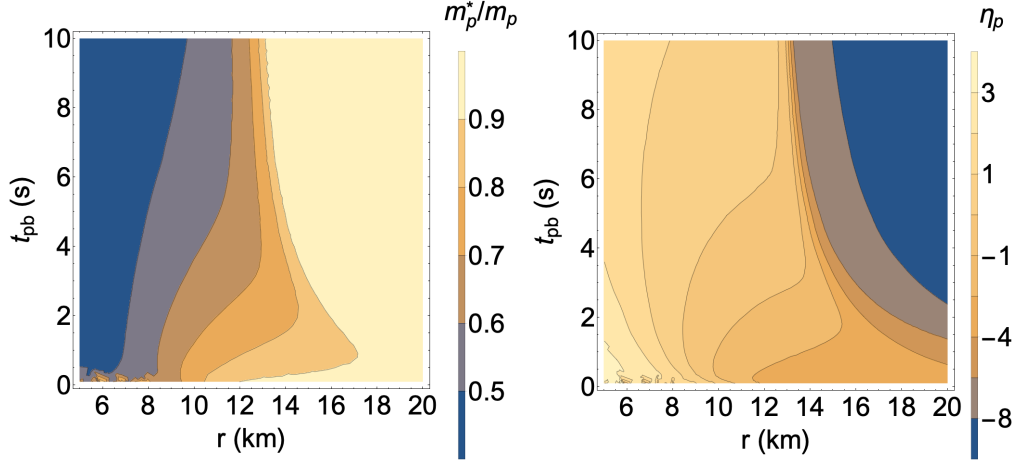


Figure 2. Isocontours of the ratio m_p^*/m_p (left panel) and of proton degeneracy parameter η_p (right panel) in the plane r – t_{pb} .

[32],

$$E(p) - \mu_p^* \approx m_p + \frac{p^2}{2m_p^*} + U_p - \mu_p, \quad (2.2)$$

with the definition of the proton mean-field potential, $U_p = \Sigma_p^V - \Sigma_p^S$, that allows us to rewrite the Fermi-Dirac distribution as follows,

$$f_p(p; \{\mu_p, T\}) \approx \left[\exp \left\{ \frac{p^2}{2m_p^* T} - \eta_p \right\} + 1 \right]^{-1}, \quad (2.3)$$

where we have introduced the proton degeneracy parameter, η_p , as follows,

$$\eta_p = \frac{\mu_p - m_p - U_p}{T}. \quad (2.4)$$

The right panel of Fig. 2 shows that protons are partly degenerate ($\eta_p > 1$) in the inner core of the proto-neutron star, ($r < 10$ km) where the nuclear saturation density ρ_{sat} is reached.

Through the distribution function of Eq. (2.3), the free-proton number density can be obtained as

$$n_p = 2\xi \int \frac{d^3\mathbf{p}}{(2\pi)^3} f_p, \quad (2.5)$$

where 2 is the spin degeneracy factor while $\xi < 1$ is the so-called “filling factor”, which refers to unbound nuclei. It is related with the excluded volume approach of Ref. [30] employed in the nuclear equation of state to account for the dissolving of nuclear clusters with increasing density, i.e. the transition to homogeneous nuclear matter. In particular, in the limit $\xi \rightarrow 0$ all protons would be collected in clusters, while for $\xi = 1$ all protons would be free. The filling factor in our reference model is shown in the left panel of Fig. 3. As evident from the figure, this does not induce substantial corrections, since $0.9 < \xi < 1$.

Finally, the proton degeneracy implies a reduction of the number of targets $n_p \rightarrow n_p^{\text{eff}}$ for the Primakoff process. In particular, since protons are fermions the effective number of

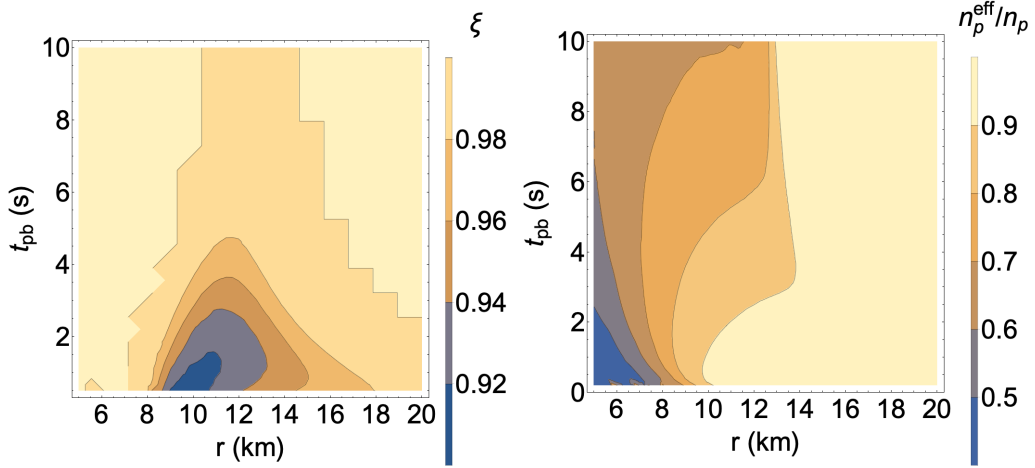


Figure 3. Isocontours of the filling factor ξ (left panel) and of the ratio n_p^{eff}/n_p (right panel) in the plane r - t_{pb} .

targets can be calculated by inserting the Pauli blocking factor $(1 - f_p)$ in the integral in Eq. (2.5). Thus n_p^{eff} results to be [17]

$$n_p^{\text{eff}} = 2\xi \int \frac{d^3\mathbf{p}}{(2\pi)^3} f_p(1 - f_p), \quad (2.6)$$

Contours of n_p^{eff}/n_p are shown in the right panel of Fig. 3 and indicate a suppression up to 50% in the inner core of the PNS, where the protons are degenerate.

2.3 Neutrino opacity

In order to characterize the axion emissivity in the trapping regime we need to compare the axion opacity with the neutrino one. The AGILE-BOLTZTRAN code provides a detailed characterization of the neutrino opacity. However, for the sake of the simplicity, since our treatment of the axion opacity will be simplified we prefer to use also for the neutrino case an approximated recipe. This has the benefit to allows for a semi-analytical calculation of the neutrino opacity.

In the standard scenario neutrinos are trapped in the SN core and are emitted from the last-scattering surface, the neutrino-sphere at radius R_ν . The strength of the neutrino interactions with matter is characterized through the opacity κ_ν , related to the mean-free path λ_ν by $\kappa_\nu \rho = 1/\lambda_\nu$. Since at early times the neutrino emissivity is dominated by electron species, the neutrino opacity can be roughly evaluated averaging the opacity of electron neutrinos and antineutrinos [34]

$$\kappa_\nu = \frac{L_{\nu_e} \kappa_{\nu_e} + L_{\bar{\nu}_e} \kappa_{\bar{\nu}_e}}{L_{\nu_e} + L_{\bar{\nu}_e}}, \quad (2.7)$$

where L_{ν_e} and $L_{\bar{\nu}_e}$ are the electron neutrino and antineutrino luminosities, while κ_{ν_e} and $\kappa_{\bar{\nu}_e}$ are the electron neutrino and antineutrino opacities, which have contributions from scattering κ_{sc} and absorption processes κ_{ab} . Following the derivation in [34], we define an effective

opacity $\kappa_{\text{eff}} = \sqrt{\kappa_{\text{ab}}(\kappa_{\text{ab}} + \kappa_{\text{sc}})}$ with a schematic expression

$$\begin{aligned}\kappa_{\nu_e} &\equiv \kappa_{\text{eff},\nu_e} = 1.62 \frac{\sigma_0 \langle E_{\nu_e}^2 \rangle}{m_e^2} \frac{1}{m_u} X_n \sqrt{1 + 0.21 \frac{X_p}{X_n}}, \\ \kappa_{\bar{\nu}_e} &\equiv \kappa_{\text{eff},\bar{\nu}_e} = 1.62 \frac{\sigma_0 \langle E_{\bar{\nu}_e}^2 \rangle}{m_e^2} \frac{1}{m_u} X_p \sqrt{1 + 0.21 \frac{X_n}{X_p}},\end{aligned}\tag{2.8}$$

where $m_u = 1.66 \times 10^{-24}$ g is the atomic mass unit, $m_e = 0.511$ MeV is the electron rest mass, $\sigma_0 = 1.76 \times 10^{-44}$ cm², X_p and X_n are the number fractions of free neutrons and protons.

2.4 The characteristic radii

The features of a SN explosion are strictly connected to three characteristic radii of the SN atmosphere: the neutrino-sphere radius R_ν , the gain radius R_{gain} and the shock radius R_s . Note that in multi-dimensional supernova simulations, these quantities do not represent perfect spheres because of the presence of multi-dimensional phenomena such as convection and rotation induced mixing. The neutrino-sphere radius R_ν can be evaluated through the opacity κ_ν in Eq. (2.7) through the relation

$$\tau_\nu(R_\nu) = \int_{R_\nu}^{\infty} \kappa_\nu \rho dr = \frac{2}{3},\tag{2.9}$$

where τ_ν is the optical depth. This condition corresponds to the requirement that a neutrino emerging from the neutrino-sphere has a probability $e^{-\tau_\nu} = e^{-2/3}$ to reach the infinity. For this reason, in a simplified way the proto-neutron star can be seen as a black-body cooling via neutrino emission from a surface of radius R_ν .

Actually, neutrino emission and absorption processes determine the cooling and the heating of the matter in the neutrino decoupling region, respectively. In particular, in the SN model of Fig. 1 charged-current, neutrino-nucleon/nucleus as well as neutrino-electron scattering and neutrino pair processes are considered (see Table (1) in Ref. [24], including the updates described in Refs. [24, 35]). The total heating rates Q_ν [in units of MeV cm⁻³ s⁻¹] are defined by the following integral expressions over the neutrino energy, E , and relative momentum angle between neutrino propagation and the radial motion, $\mu = \cos \theta$,

$$\begin{aligned}Q_{\nu_e} &= \frac{2\pi c}{(hc)^3} \int dE E^3 \int d\mu \{ \kappa_{\nu_e}(E) f_{\nu_e}(E, \mu) - j_{\nu_e}(E)(1 - f_{\nu_e}(E, \mu)) \} \\ &+ \frac{2\pi}{(hc)^3} \int dE E^2 \int d\mu \\ &\left(f_{\nu_e}(E, \mu) \frac{2\pi}{(hc)^3} \int dE' E'^2 \int d\mu' (E - E') R_{\text{scat},\nu_e}^{\text{out}}(E, E', \mu, \mu') (1 - f_{\nu_e}(E', \mu')) \right. \\ &- (1 - f_{\nu_e}(E, \mu)) \frac{2\pi}{(hc)^3} \int dE' E'^2 \int d\mu' (E - E') R_{\text{scat},\nu_e}^{\text{in}}(E, E', \mu, \mu') f_{\nu_e}(E', \mu') \\ &+ f_{\nu_e}(E, \mu) \frac{2\pi}{(hc)^3} \int dE' E'^2 \int d\mu' (E + E') R_{\nu_e\bar{\nu}_e}^{\text{a}}(E, E', \mu, \mu') f_{\bar{\nu}_e}(E', \mu') \\ &\left. - (1 - f_{\nu_e}(E, \mu)) \frac{2\pi}{(hc)^3} \int dE' E'^2 \int d\mu' (E + E') R_{\nu_e\bar{\nu}_e}^{\text{p}}(E, E', \mu, \mu') (1 - f_{\bar{\nu}_e}(E', \mu')) \right)\end{aligned}\tag{2.10}$$

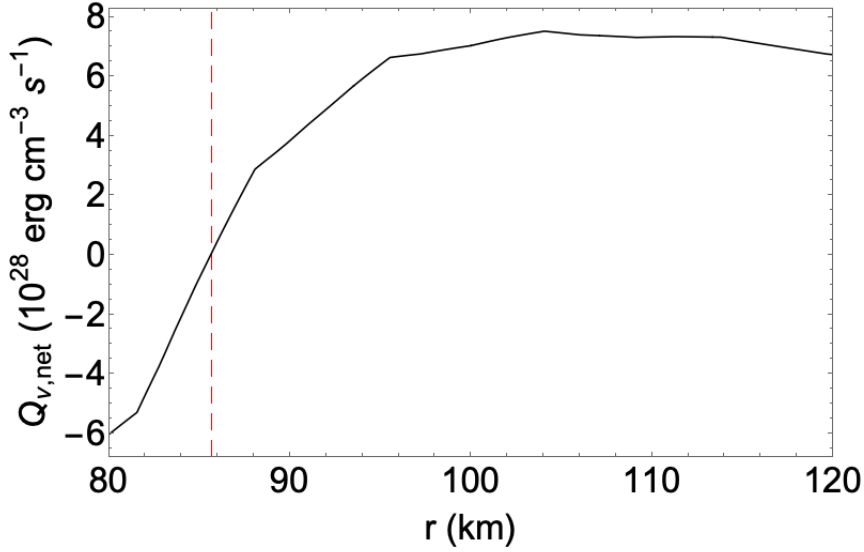


Figure 4. The net heating rate $Q_{\nu,\text{net}}$ (see text for definition) in the zone where it becomes positive at $t_{\text{pb}} = 0.3$ s. The vertical dashed red line corresponds to $R_{\text{gain}} \approx 86$ km.

of the neutrino emissivity, j_ν and opacity, κ_ν , in/out-scattering and production/absorption pair processes reaction kernels, $R_{\text{scat},\nu}^{\text{in/out}}$ and $R_{\nu\nu}^{\text{p/a}}$, taking into account the neutrino phase space occupation in the initial, $f_\nu(E, \mu)$, and final states, $f_\nu(E', \mu')$ (further details can be found Ref. [36]). The similar expression is obtained for the $\bar{\nu}_e$ heating rate, $Q_{\bar{\nu}_e}$, as well as for the heavy-lepton flavors, $Q_{\nu_{\mu/\tau}}$ and $Q_{\bar{\nu}_{\mu/\tau}}$, except that for the latter two there is no contributions from the charged-current emissivity and opacity. The total net neutrino heating rate is then obtained by summing over all neutrino flavors, denoted as $Q_{\nu,\text{net}} = Q_{\nu_e} + Q_{\bar{\nu}_e} + 2Q_{\nu_{\mu/\tau}} + 2Q_{\bar{\nu}_{\mu/\tau}}$, where the factors of 2 arise since μ - and τ -neutrinos and antineutrinos are treated as one species. Note that contributions with a + sign belong to the total neutrino heating rate, denoted as Q_ν^+ , while those with a - sign belong to the cooling rate, denoted as Q_ν^- . It is useful to define the gain radius, R_{gain} , as the radius at which the neutrino heating balances the cooling, i.e. the net heating rate $Q_{\nu,\text{net}} \equiv Q_\nu^+ - Q_\nu^-$ vanishes, as shown in Fig. 4 for $t_{\text{pb}} = 0.3$ s. According to this definition, for $R < R_{\text{gain}}$ neutrino production prevails, $Q_\nu^+ < Q_\nu^-$, while at larger distances the absorption processes dominate.

In the so-called neutrino-driven explosion scenario, the energy deposited at early times ($t_{\text{pb}} \lesssim 0.3$ s) in the “gain layer”, i.e. the region between R_{gain} and the position of the shock-wave front R_s , triggers the SN explosion. For this reason it is of crucial importance to evaluate the time evolution of the shock radius R_s , beyond which the matter is not yet uncompressed.

In Fig. 5 we show the time evolution from $t_{\text{pb}} = 10$ ms to $t_{\text{pb}} = 1$ s of the three characteristic radii. We observe that the neutrino-sphere radius (the continuous black curve) is ~ 50 km at early times ($t_{\text{pb}} \lesssim 100$ ms) and it decreases to ~ 20 km at $t_{\text{pb}} = 1$ s. The gain radius R_{gain} (the dashed black curve) has a similar evolution. More specifically, $R_{\text{gain}} \sim O(100 \text{ km})$ in the first 0.3 s after the core-bounce (in agreement with literature estimate [34]), but it starts decreasing all the way to $R_{\text{gain}} \approx 23$ km at $t_{\text{pb}} = 1$ s. The time evolution of the shock radius R_s is peculiar of a 1-D simulated SN explosion. It increases until $t_{\text{pb}} \approx 200$ ms but at larger times it starts receding. After the artificial enhancement

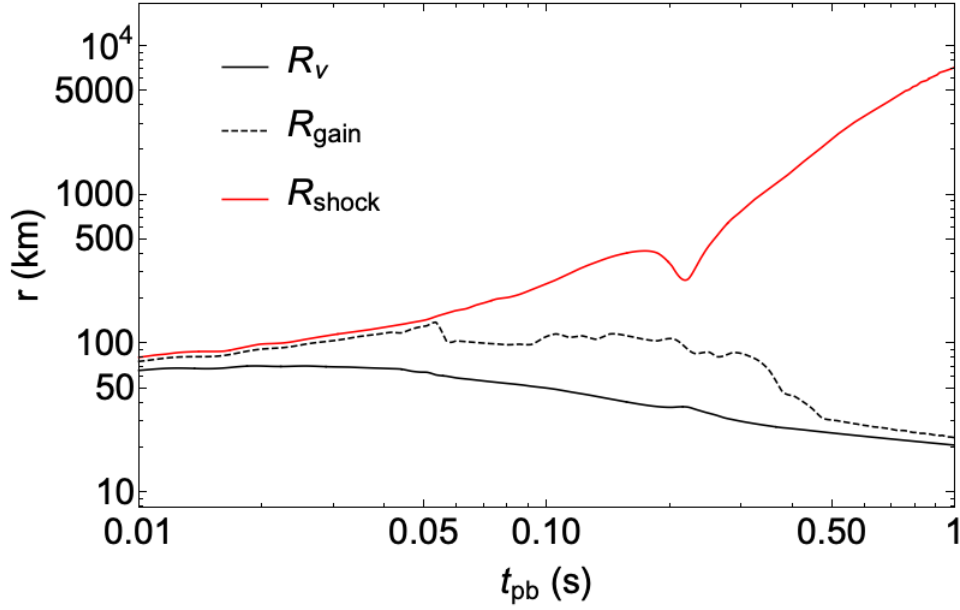


Figure 5. Time evolution of the neutrino-sphere radius R_ν (continuous black line), the gain radius R_{gain} (dashed black line) and the shock radius R_{shock} (continuous red curve).

of the deposited energy in the gain layer, the SN explosion is triggered and thus the shock radius begins to grow again, reaching $R_s \gtrsim O(10^3 \text{ km})$ at times larger than $t_{\text{pb}} \approx 0.5 \text{ s}$.

3 ALP emissivity in a supernova

3.1 Primakoff process

The two-photon coupling of ALPs [37]

$$\mathcal{L}_{a\gamma\gamma} = -\frac{1}{4}g_{a\gamma}a\tilde{F}^{\mu\nu}F_{\mu\nu} \ , \quad (3.1)$$

allows for ALP production in a SN via the Primakoff process, i.e. the conversion of a photon into an ALP in the electric field of nuclei or electrons in the stellar matter. In the case of massive ALPs the Primakoff transition rate is given by [9, 12, 38]

$$\Gamma_{\gamma \rightarrow a} = g_{a\gamma}^2 \frac{T\kappa_s^2}{32\pi} \frac{p}{E} \left\{ \frac{\left[(k+p)^2 + \kappa_s^2 \right] \left[(k-p)^2 + \kappa_s^2 \right]}{4kp\kappa_s^2} \ln \left[\frac{(k+p)^2 + \kappa_s^2}{(k-p)^2 + \kappa_s^2} \right] - \frac{(k^2 - p^2)^2}{4kp\kappa_s^2} \ln \left[\frac{(k+p)^2}{(k-p)^2} \right] - 1 \right\} , \quad (3.2)$$

where $p = \sqrt{E^2 - m_a^2}$ and $k = \sqrt{\omega^2 - \omega_{\text{pl}}^2}$ are the ALP and photon momentum respectively, while the plasma frequency $\omega_{\text{pl}} \simeq 16.3 \text{ MeV } Y_e^{1/3} \rho_{14}^{1/3}$ [39], where $\rho_{14} = \rho/10^{14} \text{ g cm}^{-3}$ and Y_e is the electron fraction, plays the role of an “effective photon mass”. We take $E = \omega$ since the energy is conserved. Finally, κ_s is an appropriate screening scale which accounts for the finite range of the electric field of the charged particles in the stellar medium. In a SN core, the most substantial contribution to the ALP emission via Primakoff comes from

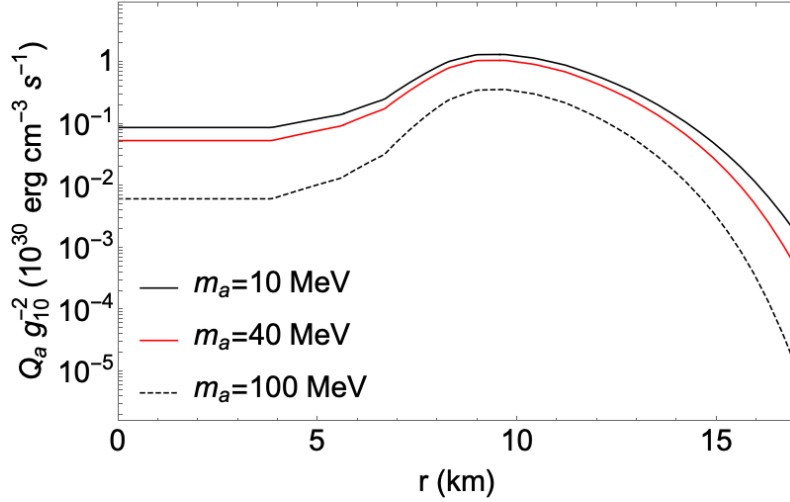


Figure 6. ALP emissivity at $t_{\text{pb}} = 1$ s for different values of the ALP mass m_a , as shown in legend.

free protons. Indeed, electrons are highly degenerate in the SN core. Thus the electron phase space is Pauli-blocked and hence their contribution to the ALP production is negligible. On the other hand, protons are only partially degenerate, as shown in the right panel of Fig. 2. For this reason, only proton contribution to the Primakoff rate is considered. In the non-degenerate regime, the screening scale would be the Debye one, but in this case, in order to take into account the partial proton degeneracy, the appropriate choice for the inverse screening length is [17]

$$\kappa_s^2 = \frac{4\pi\alpha n_p^{\text{eff}}}{T}, \quad (3.3)$$

with n_p^{eff} given by Eq. (2.6). Note that a larger degeneracy implies the reduction of the effective number density of the targets and therefore the strength of the Primakoff rate is suppressed.

In order to evaluate the energy-loss by Primakoff production, one has to calculate the ALP emissivity Q_a , in units of $\text{erg cm}^{-3} \text{s}^{-1}$, which represents the energy emitted via ALP production per unit volume and time. It results

$$Q_a = 2 \int \frac{d^3\mathbf{k}}{(2\pi)^3} \Gamma_{\gamma \rightarrow a} \omega f(\omega) = \int_{m_a}^{\infty} dE E \frac{d^2 n_a}{dt dE}, \quad (3.4)$$

where the factor 2 comes from the photon polarization degrees of freedom and $f(\omega) = (e^{\omega/T} - 1)^{-1}$ is the Bose-Einstein distribution function of the thermal photons. At fixed mass m_a , the emissivity is larger at values of the radius r where the temperature T is higher. In Fig. 6 we show the ALP emissivity for different values of the ALP mass at $t_{\text{pb}} = 1$ s, normalized to the square of the ALP-photon coupling $g_{10} = g_{a\gamma}/10^{-10} \text{ GeV}^{-1}$. It is evident that, regardless of the mass m_a , the region of larger production is between $r \sim 5 - 15$ km, and the peak of the ALP emissivity is attained at $r \sim 10$ km, where the temperature reaches its maximum value, as shown in Fig. 1 (left panel). It is also noticeable the Boltzmann suppression of the ALP emissivity, induced by the factor $e^{-m_a/T}$, as the mass increases.

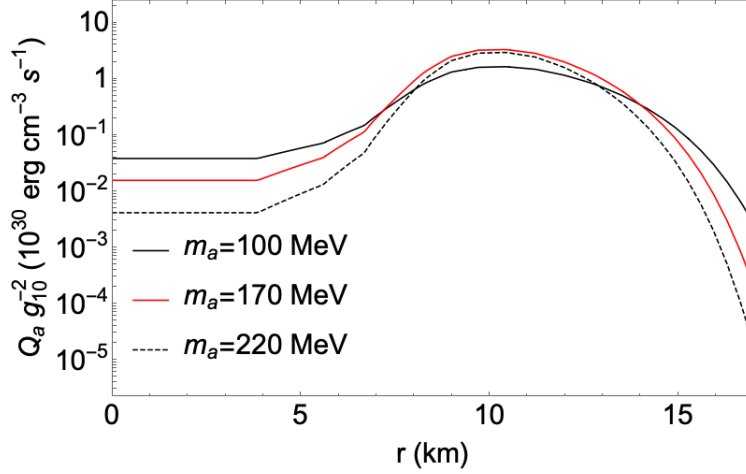


Figure 7. ALP emissivity from photon coalescence for different values of the ALP mass at $t_{\text{pb}} = 1$ s.

3.2 Photon coalescence

In a medium of sufficiently high density, ALPs can also be produced through the so-called “photon coalescence” or “inverse decay process” [38], where two photons can annihilate producing an axion. This process has a kinematic threshold, vanishing for $m_a < 2\omega_{\text{pl}}$.

In order to evaluate the axion production rate from photon coalescence in a thermal medium, it is convenient to approximate the Bose-Einstein photon distribution with a Maxwell-Boltzmann $f(E) \rightarrow e^{-E/T}$ for the photon occupation number [38]. The approximation is well justified since, at masses for which the coalescence process dominates, $m_a \gtrsim 100$ MeV, $E \geq m_a \gg T$. Thus, the production rate per unit volume and energy can be expressed as [12]

$$\frac{d^2 n_a}{dt dE} = g_{a\gamma}^2 \frac{m_a^4}{128\pi^3} p \left(1 - \frac{4\omega_{\text{pl}}^2}{m_a^2} \right)^{3/2} e^{-E/T}, \quad (3.5)$$

with $p = \sqrt{E^2 - m_a^2}$. The axion emissivity can be calculated as before

$$Q_a = \int_{m_a}^{\infty} dE E \frac{d^2 n_a}{dt dE}. \quad (3.6)$$

At fixed value of the axion mass m_a , the emissivity is larger at radii r where the temperature is higher because of the Boltzmann factor in Eq. (3.5). The ALP emissivities for different values of the mass m_a at $t_{\text{pb}} = 1$ s are shown in Fig. 7. Regardless of the axion mass, the emissivity is maximal at $r \approx 10$ km and the production region via photon coalescence is the same as Primakoff, between $r \approx 5 - 15$ km. As depicted in Fig. 7, in the production region the emissivity increases until $m_a \approx 170$ MeV and then it starts decreasing because of the Boltzmann suppression, while outside this region the ALP production is strongly suppressed for any mass value.

Finally, the ALP luminosity, i.e. the energy emitted per unit time (measured in erg s⁻¹), is given integrating the emissivity over the SN model, i.e.

$$L_a = 4\pi \int Q_a(r) r^2 dr. \quad (3.7)$$

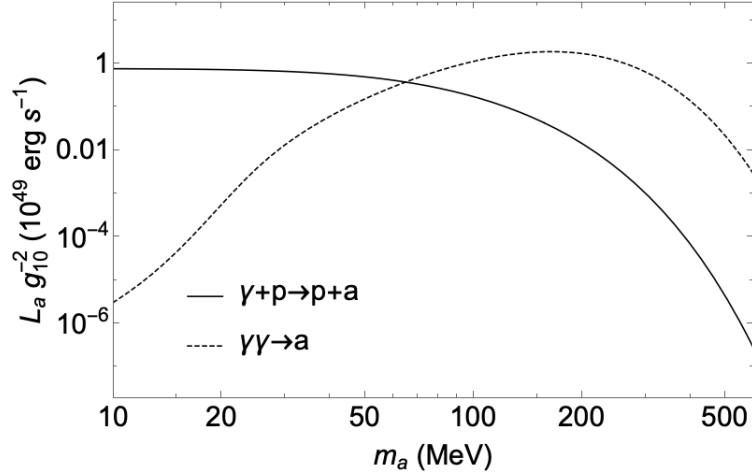


Figure 8. ALP luminosity for Primakoff (continuous curve) and photon coalescence (dashed curve) as a function of the axion mass m_a at $t_{\text{pb}} = 1$ s.

In Fig. 8 the axion luminosities from Primakoff and photon coalescence as a function of the axion mass m_a at $t_{\text{pb}} = 1$ s are represented. It is apparent that the coalescence process is sub-leading for $m_a \lesssim 70$ MeV, while at larger masses it becomes dominant and reaches its maximum at $m_a \approx 170$ MeV.

4 SN 1987A ALP bounds

4.1 Free-streaming regime

4.1.1 Energy-loss argument

The SN 1987A neutrino observations by KII and IMB experiments are in good agreement with the standard picture of proto-neutron star (PNS) cooling by neutrinos on a time scale of $\mathcal{O}(10$ s) (see, e.g., [40]). If ALPs with mean free path larger than the proto-neutron star radius were emitted from the interior of the SN, they would provide a very efficient new cooling mechanism. Observationally, this implies that the cooling time scale would be shortened. In particular, the observed duration of the neutrino signal precludes the ALP luminosity L_a to exceed the neutrino luminosity in all the six (anti)neutrino degrees of freedom L_ν in the cooling phase. Conventionally, it is taken as benchmark the neutrino luminosity value at $t_{\text{pb}} = 1$ s, $L_\nu(t_{\text{pb}} \sim 1 \text{ s}) \simeq 3 \times 10^{52} \text{ erg s}^{-1}$. Thus, the constraint on ALP emissivity is obtained requiring [41]

$$L_a(t_{\text{pb}} = 1 \text{ s}) \lesssim 3 \times 10^{52} \text{ erg s}^{-1}. \quad (4.1)$$

We stress that several numerical simulations have shown that the duration of the neutrino burst would be roughly halved when the limit (4.1) is saturated [41].

Imposing that the total ALP luminosity satisfies Eq. (4.1) provides a constraint on the ALP-photon coupling $g_{a\gamma}$ as a function of the ALP mass m_a . Our result is shown in the exclusion plot reported in Fig. 9, in which the area shaded in light red, delimited by a continuous black line, represents the ALP parameter region excluded through the energy-loss argument. In the low-mass limit ($m_a \lesssim$ a few MeV), where the photon coalescence is not relevant, values of the ALP-photon coupling $g_{a\gamma} \gtrsim 6 \times 10^{-9} \text{ GeV}^{-1}$ are excluded, in agreement with previous results [19]. A comparison of the continuous line with the dashed black curve, which shows

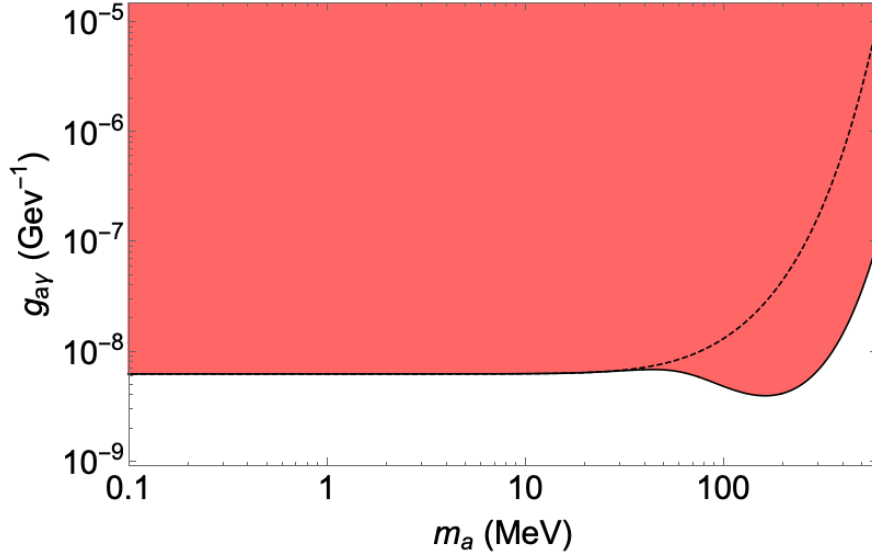


Figure 9. ALP exclusion plot in the $g_{a\gamma} - m_a$ plane coming from the energy-loss argument. The dashed black curve represents the bound accounting the ALP emissivity by only Primakoff process while the continuous black curve includes also the photon coalescence process.

the bound obtained assuming only the Primakoff process, reveals that for masses above a few 10 MeV the photon coalescence is no longer negligible. Indeed, including this channel the bound is strengthened by a factor $\gtrsim 3$ for $m_a \gtrsim 100$ MeV and by over an order of magnitude for $m_a \gtrsim 200$ MeV. We note that for masses $m_a \gtrsim 170$ MeV the bound is weakened since the ALP production is Boltzmann-suppressed.

4.1.2 Gravitational trapping

ALPs produced with a kinetic energy satisfying

$$E_{\text{kin}} \leq K_{\text{tr}} \equiv \frac{G_{\text{N}} M_r m_a}{r}, \quad (4.2)$$

will not free stream, since they are trapped by gravitational attraction [42]. In Eq. (4.2), G_{N} is the Newton constant, r is the radius at which the ALP is produced and M_r is the mass of supernova enclosed within the radius r . One can schematically include this effect by modifying the ALP volume emission rate per unit energy as

$$\frac{d^2 n_a}{dE dt} \rightarrow \frac{d^2 n_a}{dE dt} \theta(E - m_a - K_{\text{tr}}). \quad (4.3)$$

At $t_{\text{pb}} = 1$ s, the gravitational potential $U_G(r) = \frac{G_{\text{N}} M_r}{r}$ has a maximum at $r_{\text{max}} \simeq 17$ km, where $U_G(r_{\text{max}}) = U_{\text{max}} \simeq 0.12$. Therefore ALPs produced at $r \leq r_{\text{max}}$ must have a kinetic energy $E_{\text{kin}} > m_a U_{\text{max}}$ in order to escape from the potential well, otherwise they will be gravitationally trapped. For this reason the effect of the gravitational trapping is accounted

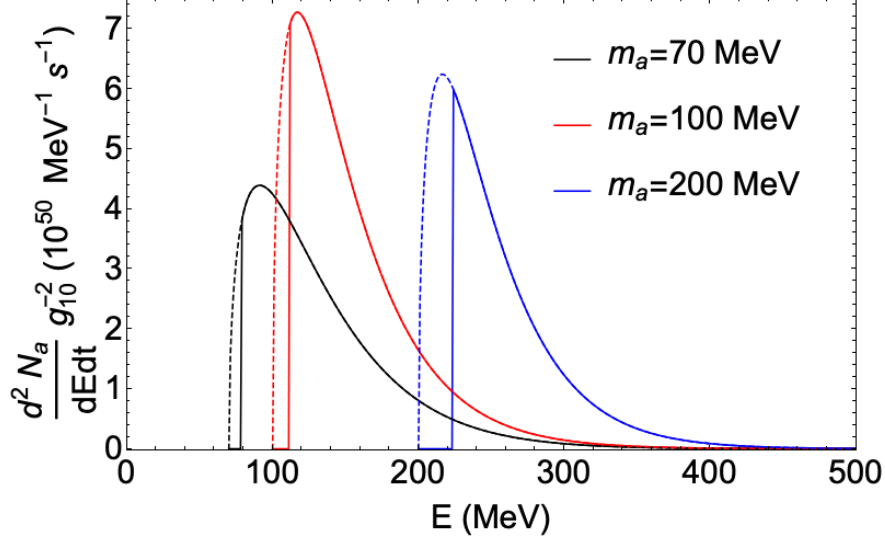


Figure 10. Total ALP production rate per unit energy at $t_{\text{pb}} = 1$ s for $m_a = 70$ MeV (black curves), $m_a = 100$ MeV (red curves) and $m_a = 200$ MeV (blue curves). The dashed curves refer to cases without the inclusion of the gravitational trapping effect, which is accounted for in the continuous curves.

in the ALP emissivity as

$$\frac{d^2 n_{a, \text{tr}}}{dE dt} = \begin{cases} \frac{d^2 n_a}{dE dt} \theta(E - m_a - m_a U_{\text{max}}) & \text{if } r \leq r_{\text{max}} , \\ \frac{d^2 n_a}{dE dt} \theta(E - m_a - K_{\text{tr}}) & \text{if } r > r_{\text{max}} . \end{cases} \quad (4.4)$$

With this prescription we can compute the emissivity Q_a in Eq. (3.4) and the luminosity L_a in Eq. (3.7). We stress that, since at $t_{\text{pb}} = 1$ s the ALP production region is in the region $r \in [5; 15]$ km, essentially all the ALPs must satisfy the condition in the first line of Eq. (4.4). This implies that at fixed mass m_a the total ALP emission rate per unit energy would be cut for $E_a \lesssim 1.12 m_a$ because of the gravitational attraction, as shown in Fig. 10. It is evident that this effect becomes more important as the ALP mass m_a increases, thus the energy-loss bound results to be relaxed at larger masses, as depicted in Fig. 11 (upper panel). In particular, for $m_a \lesssim 100$ MeV the gravitational trapping is negligible, while the bound is relaxed by $\gtrsim 15\%$ for $m_a \gtrsim 200$ MeV, as shown in Fig. 11 (lower panel).

4.2 Trapping regime

As the ALP-photon coupling $g_{a\gamma}$ increases, ALPs are trapped in the SN core when their mean free path (mfp) becomes smaller than the size of the SN core ($R_c \sim 10$ km). In this case, they would remove energy from one region of the star and deposit it at an approximate distance of one mfp. Thus they may contribute significantly to the energy transport, modifying the SN evolution. Here, we closely follow the approach of Ref. [43]. One defines the ALP Rosseland mfp as $\lambda_a = (\kappa_a \rho)^{-1}$ in terms of the Rosseland opacity

$$\kappa_a^{-1} = \frac{\int_{m_a}^{\infty} \kappa_E^{-1} \beta_E \partial_T B_E dE}{\int_{m_a}^{\infty} \beta_E \partial_T B_E dE} , \quad (4.5)$$

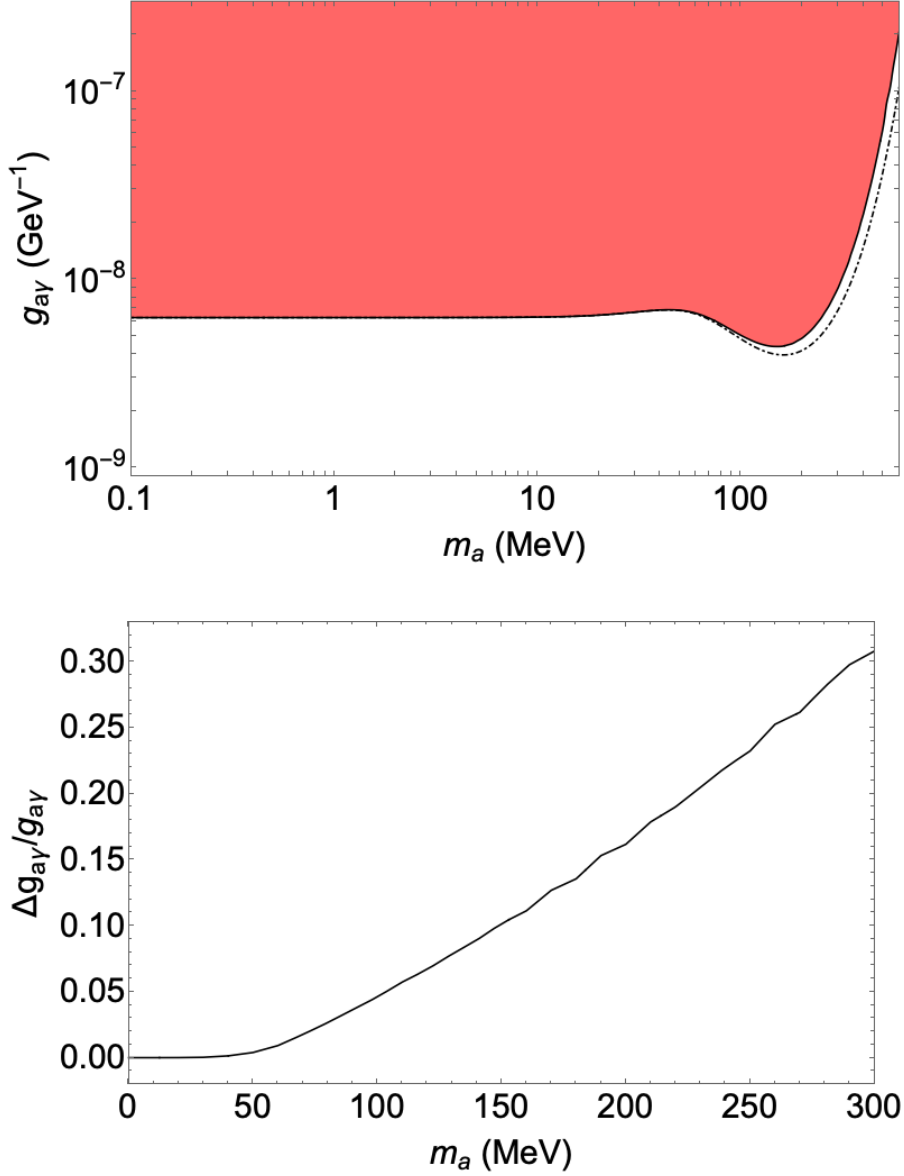


Figure 11. *Upper panel:* ALP exclusion plot from the energy-loss argument in the plane $g_{a\gamma} - m_a$. The continuous black curve includes the gravitational trapping effect, which is ignored in the dash-dotted black curve. *Lower panel:* The discrepancy between the bound on the coupling $g_{a\gamma}$ evaluated accounting the gravitational trapping effect and the one obtained by ignoring this effect.

where

$$B_E = \frac{1}{2\pi^2} \frac{E^2(E^2 - m_a^2)^{1/2}}{e^{E/T} - 1} , \quad (4.6)$$

is the ALP thermal spectrum and the ALP opacity κ_E is evaluated by considering in Eq. (4.5) the contributions of the inverse Primakoff effect $a + p \rightarrow p + \gamma$ and the decay process $a \rightarrow \gamma\gamma$

$$\kappa_E = \kappa_{a \rightarrow \gamma} + \kappa_{a \rightarrow \gamma\gamma} . \quad (4.7)$$

The decay contribution $\kappa_{a \rightarrow \gamma\gamma}$ results to be

$$\kappa_{a \rightarrow \gamma\gamma} = \frac{1}{\rho \lambda_{a \rightarrow \gamma\gamma}} = \frac{1}{\rho} \frac{\Gamma_{a \rightarrow \gamma\gamma}}{\beta_E \gamma_E}, \quad (4.8)$$

where $\lambda_{a \rightarrow \gamma\gamma}$ is the decay mfp, $\gamma_E = E/m_a$ is the Lorentz factor, $\beta_E = \sqrt{1 - \gamma_E^{-2}}$ and $\Gamma_{a \rightarrow \gamma\gamma}$ is the decay rate

$$\Gamma_{a \rightarrow \gamma\gamma} = g_{a\gamma}^2 \frac{m_a^3}{64\pi} \left(1 - \frac{4\omega_{\text{pl}}^2}{m_a^2}\right)^{3/2}. \quad (4.9)$$

On the other hand, the inverse Primakoff contribution $\kappa_{a \rightarrow \gamma}$ results to be

$$\kappa_{a \rightarrow \gamma} = \frac{1}{\rho \lambda_{a \rightarrow \gamma}} = \frac{1}{\rho} \frac{\Gamma_{a \rightarrow \gamma}}{\beta_E}, \quad (4.10)$$

where $\lambda_{a \rightarrow \gamma}$ is the inverse Primakoff mfp and $\Gamma_{a \rightarrow \gamma} = (2\beta_\gamma/\beta_E)\Gamma_{\gamma \rightarrow a}$ is the inverse Primakoff rate, with $\Gamma_{\gamma \rightarrow a}$ given by Eq. (3.2), and the factor 2 accounting for the photon polarization.

When the ALPs mass is less than few MeV, the inverse Primakoff process dominates over the decay, which has a strong dependence on the axion mass (m_a^3) and is forbidden for $m_a < 2\omega_{\text{pl}}$. Since the Primakoff opacity is strictly dependent on the matter density ρ , in the low-mass limit ALPs are trapped in the inner SN core and they are emitted from an “axion-sphere”, which is the analogous of the “neutrino-sphere”. More specifically, the radius of the axion-sphere R_a is determined by the condition

$$\tau_a(R_a) = \int_{R_a}^{\infty} \kappa_a \rho dr = \frac{2}{3}, \quad (4.11)$$

where κ_a is the Rosseland mean opacity defined in Eq. (4.5). Therefore, for masses $m_a \lesssim O(1 \text{ MeV})$, trapped ALPs are expected to have a black-body emission with a luminosity $L_a \propto R_a^2 T^4(R_a)$. The bound on the coupling $g_{a\gamma}$ is obtained by imposing [44]

$$L_a \lesssim L_\nu. \quad (4.12)$$

As in the case of the free-streaming regime, we are concerned mostly with the SN cooling phase ($t_{\text{pb}} \gtrsim 0.5 \text{ s}$), when the outer core has settled and the shock has begun to escape. Specifically, in order to constrain the ALP parameter space in the trapping regime we consider the SN model of Fig. 1 at a representative time $t_{\text{pb}} = 1 \text{ s}$. This condition excludes the values of the photon-axion coupling $g_{a\gamma} \lesssim 7.7 \times 10^{-6} \text{ GeV}^{-1}$, in agreement with Ref. [8].

For heavier ALPs, $m_a \gtrsim 10 \text{ MeV}$, the decay process becomes dominant. This implies that at these masses the “axion-sphere” cannot be well defined because the integral in Eq. (4.11) always diverges since the decay mfp tends to a constant value in vacuum. In this context, ALPs may decay before leaving the SN core, contributing to the energy transfer. In order to constrain $g_{a\gamma}$ one should impose at the neutrinosphere R_ν that

$$\kappa_a \gtrsim \kappa_\nu, \quad (4.13)$$

where κ_ν is the neutrino opacity, given by Eqs. (2.7)–(2.8). The bound obtained following this approach has been connected with the one for the low-mass case dominated by the Primakoff process, computed through Eq. (4.12). The resulting constraint is constant in the low-mass

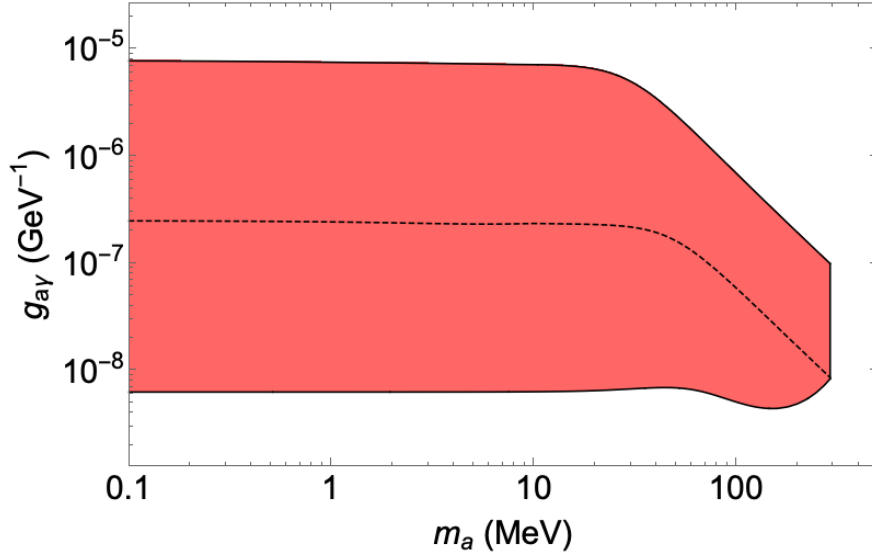


Figure 12. Exclusion plot in the plane m_a - $g_{a\gamma}$ obtained by combining the energy-loss argument (lower boundary) and the energy-transfer argument (upper boundary). The dashed black line represents the border between the free-streaming and trapping regimes.

limit $m_a \lesssim 10$ MeV while for higher masses it decreases as $\sim m_a^{-3/2}$, as shown in Fig. 12. The shaded red region in Fig. 12 is the zone excluded by combining the energy-loss and the energy-transfer arguments, while the dashed black line represents the border between the free-streaming (lower $g_{a\gamma}$) and the trapping regime (higher $g_{a\gamma}$), obtained by imposing the condition [43]

$$\tau_a(R_p, R_\nu) = \int_{R_p}^{R_\nu} dr \kappa_a \rho = 1, \quad (4.14)$$

where R_p is the mean radius at which the axion are produced

$$R_p = \frac{\int dr r Q_a(r)}{\int dr Q_a(r)}. \quad (4.15)$$

The condition in Eq. (4.14) corresponds to the requirement that an ALP produced at R_p should emerge from the neutrino-sphere, with a survival probability e^{-1} . Since the dashed line intersects the free-streaming bound at $m_a \approx 290$ MeV, the energy-loss argument is no more reliable for higher masses, which is the reason why the exclusion region has been cut with a vertical line at this value of the mass.

4.3 Modified luminosity criterion

An alternative method to constrain the ALP parameter space has been recently proposed in [45, 46]. This is based on the fact that only the ALP luminosity that cannot be reprocessed efficiently as neutrino energy is relevant to place a bound. More precisely, if ALPs are produced in the zone of neutrino diffusion, i.e. behind the neutrino-sphere, energy is taken away from there. However, if they are absorbed in a region where the neutrino production is still efficient, the energy they deposit could be re-emitted via neutrino production and the neutrino signal would result to be practically unaltered. On the other hand, if ALPs reach a radius $R_{\text{far}} > R_\nu$ beyond which the neutrino production is negligible, the deposited energy

would result to be essentially unavailable to them. For this reason, the axion luminosity can be evaluated by including an optical depth factor characterizing the probability that an ALP produced in the core region ($r \lesssim R_\nu$) reaches the radius R_{far} . There is a number of reasonable choices for R_{far} , the only stringent condition being that $R_{\text{far}} > R_\nu$. A lower bound on R_{far} is the neutrino gain radius R_{gain} , outside of which neutrino production has a lower rate than the absorption one. On the other hand, a reasonable upper limit is the shock radius R_{shock} , outside of which matter is not yet uncompressed. In this work, we fix $R_{\text{far}} = R_{\text{gain}}$. From our simulation at $t_{\text{pb}} = 1$ s we find $R_{\text{gain}} \approx 23$ km, as shown in Fig. 5.

For a fixed value of R_{far} , the ALP luminosity L_a results to be [45]

$$L_a = 4\pi \int_0^{R_\nu} dr r^2 \int_{m_a}^\infty dE E \frac{d^2 n_a}{dt dE} e^{-\tau_a(r, E, R_{\text{far}})}, \quad (4.16)$$

where the volume integration is till R_ν since we are interested just in the energy taken away from behind the neutrino-sphere and the ALP volume emission rate per unit energy is given by Eq. (4.4). On the other hand, $\tau_a(r, E, R_{\text{far}})$, the optical depth of an ALP produced at r with energy E reaching R_{far} , results to be [45]²

$$\tau_a(r, E, R_{\text{far}}) = \left(1 - \frac{r(r - R_c)}{2R_\nu^2}\right) \int_r^{R_{\text{far}}} \frac{d\tilde{r}}{\lambda_a(E, \tilde{r})}, \quad (4.17)$$

where $R_c \approx 10$ km is the core radius and λ_a is the total axion mfp

$$\lambda_a^{-1} = \lambda_{a \rightarrow \gamma}^{-1} + \lambda_{a \rightarrow \gamma\gamma}^{-1}, \quad (4.18)$$

with $\lambda_{a \rightarrow \gamma}$ the inverse Primakoff mfp obtainable from Eq. (4.10) and $\lambda_{a \rightarrow \gamma\gamma}$ the decay mfp in Eq. (4.8). Since the integration over the energy in Eq. (4.16) influences the optical depth τ_a , for computational reasons we decided to define a mean optical depth τ_a^*

$$\tau_a^*(r, R_{\text{far}}) \equiv \tau_a(r, \langle E_a \rangle, R_{\text{far}}) \quad (4.19)$$

where $\langle E_a \rangle$ is the average axion energy over the emission spectrum.

Therefore the luminosity can be rewritten as

$$L_a = 4\pi \int_0^{R_\nu} dr r^2 e^{-\tau_a^*(r, R_{\text{far}})} \int_{m_a}^\infty dE E \frac{d^2 n_a}{dt dE} \equiv 4\pi \int_0^{R_\nu} dr r^2 Q_a(r) e^{-\tau_a^*(r, R_{\text{far}})}, \quad (4.20)$$

which is exactly the same expression in Eq. (3.7) modified with the inclusion of the optical depth factor $e^{-\tau_a^*}$. Thus the luminosity is essentially determined by the product of two factors: the emissivity Q_a , taking into account the axion production processes, and the optical depth factor $e^{-\tau_a^*}$, representing the axion absorption processes. Since both Q_a and τ_a increases as $g_{a\gamma}^2$, the luminosity L_a depends on the coupling constant $g_{a\gamma}$ as $L_a \sim g_{a\gamma}^2 e^{-g_{a\gamma}^2}$. For this reason at fixed value of the axion mass m_a , there are two critical values of the coupling $g_{a\gamma}$: $g_{a\gamma}^{\text{L}}$ and $g_{a\gamma}^{\text{H}}$, where the superscripts “L” and “H” stand respectively for “low” and “high”. For $g_{a\gamma} < g_{a\gamma}^{\text{L}}$, ALPs are so weakly coupled that they cannot be produced readily enough to affect the evolution of the PNS. On the other hand, for $g_{a\gamma} > g_{a\gamma}^{\text{H}}$ ALPs are trapped before they reach R_{far} , allowing the deposited energy to be efficiently reconverted in the form of thermal neutrinos. As shown in Fig. 13, for all the values in the range $g_{a\gamma}^{\text{L}} \leq g_{a\gamma} \leq g_{a\gamma}^{\text{H}}$ the

²The pre-factor $\left(1 - \frac{r(r - R_c)}{2R_\nu^2}\right)$ takes into account the non-radial trajectories, but it does not deviate substantially from one [45].

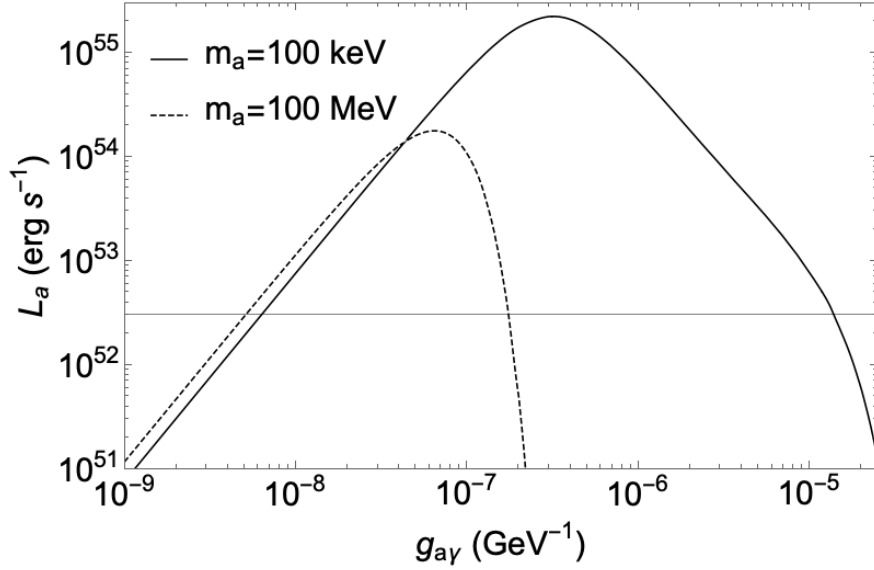


Figure 13. ALP luminosity in Eq. (4.20) as a function of the coupling constant $g_{a\gamma}$ for $m_a = 100$ keV (continuous black curve) and $m_a = 100$ MeV (dashed black curve), evaluated at $t_{\text{pb}} = 1$ s with $R_{\text{far}} = R_{\text{gain}} \approx 23$ km. The horizontal continuous black line is the critical value $L_\nu = 3 \times 10^{52}$ erg s $^{-1}$.

axion luminosity L_a violates the bound $L_a \lesssim L_\nu$ and thus these values must be excluded. This implies that in this treatment there is no reason to separate the calculation of ALP emission in a free-streaming and trapping regime since the upper and lower bounds on the coupling $g_{a\gamma}$ are determined by the optical depth factor itself.

In Fig. 14 we compare the exclusion plot obtained with the modified luminosity criterion (shaded blue region), with the region excluded combining the energy-loss and the energy-transfer argument (shaded red region). We notice that both criteria provide essentially the same results in the free-streaming regime, where the optical depth factor $e^{-\tau_a} \approx 1$, excluding the values of the coupling constant $g_{a\gamma} \gtrsim 6 \times 10^{-9}$ GeV $^{-1}$. Conversely, different results are obtained in the trapping regime. In particular, in the low-mass limit ($m_a \lesssim 10$ MeV) the modified luminosity criterion allows to exclude values of the coupling up to $g_{a\gamma} \lesssim 10^{-5}$ GeV $^{-1}$, larger than those excluded by evaluating the ALP emission at the axion-sphere radius in Eq. (4.11). As a matter of fact, in Eq. (4.12), since the decay process is negligible for $m_a \lesssim 10$ MeV, axions are assumed to be thermally emitted from the axion-sphere, underestimating the “real” ALP luminosity, evaluated through Eq. (4.16). On the other hand, for higher values of the axion mass ($m_a \gtrsim 10$ MeV), where the decay is the dominant process, the bound obtained through Eq. (4.16) is less stringent than the one obtained through the energy-transfer argument in Eq. (4.13). Indeed, the modified luminosity criterion allows to exclude values of the coupling constant $g_{a\gamma}$ for which ALPs carry too much energy beyond R_{far} but does not give any constraint for larger values of $g_{a\gamma}$ for which ALPs are trapped in the SN core and contribute to the energy transfer in the proto-neutron star. On the other hand, the energy-transfer argument allows to exclude values of the coupling for which the ALPs interact so strongly that they cannot reach R_{far} and their contribution to the energy transfer is even larger than the neutrino one. Thus the bound obtained with this latter method is more stringent for larger ALP masses. We stress that the use of different

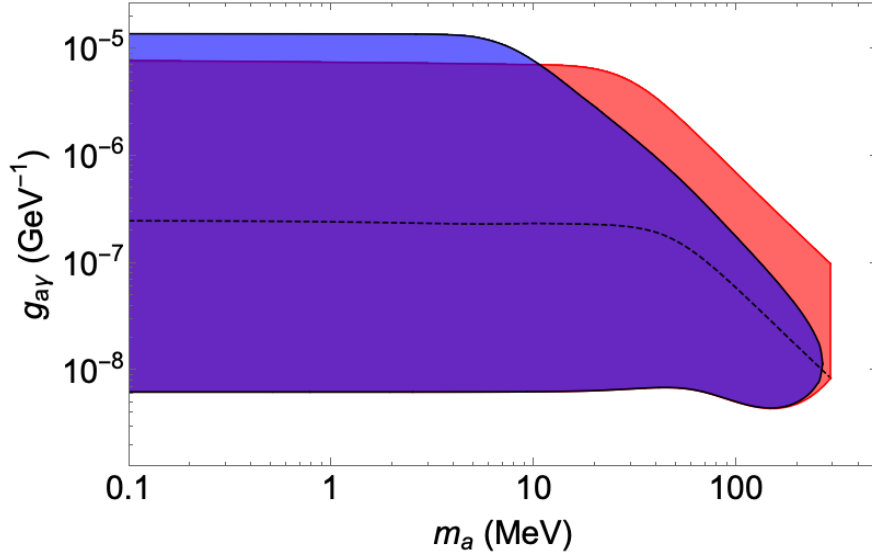


Figure 14. Region in the ALP parameter space excluded through the modified luminosity criterion (shaded blue region), compared to the region excluded by combining the energy-loss and the energy-transfer arguments (shaded red region).

strategies is necessary to take into account the effect of the axion decay in the SN core, which becomes more relevant as the axion mass increases. As expected, the comparison of the two methods to obtain bounds on the ALP parameter space shows that the lower boundary of the excluded region is more robust than the upper one, which depends on the criterion used to evaluate it and is subject to a larger uncertainty. In particular, if the upper bound is obtained through the modified luminosity criterion, it is strictly connected to the chosen value for R_{far} : an higher value of R_{far} implies a less stringent upper boundary. On the other hand, the bound obtained by limiting the energy transfer depends on the way in which the neutrino and ALP opacities are evaluated and the radius at which they are compared. The different results obtained using different criteria show that a self-consistent inclusion of ALPs in a SN simulation is necessary to have a reliable bound on the ALP parameter space, especially in the trapping regime. Performing such a simulation would be a challenging task (see, e.g., Ref. [47] for a recent investigation in the context of dark photons), and demands a separated investigation.

5 Shock revival and ALP energy deposition

Due to the photo-dissociation of heavy nuclei the SN shock wave loses its strength and after $t_{\text{pb}} \sim 100$ ms it stalls and would eventually fall back on the SN core, if it is not revitalized by some energy injection. In the “neutrino-driven explosion scenario,” the shock is revived by neutrino heating aided by multidimensional hydrodynamical effects [48], ultimately leading to a SN explosion. However, in one-dimensional simulations the heating rates for neutrino reactions are artificially increased inside the heating region to trigger the explosion. Here we investigate the intriguing possibility that the ALP production in the SN core and their subsequent decay inside the mantle would heat the SN matter and increase the total energy of the envelope, helping the revival of the shock and the trigger of the explosion even in one dimensional simulations. Indeed, ALPs decaying into photons would provide a pressure

gradient and an energy deposition in the region behind the shock, since photons quickly thermalize with matter. An amount of energy E_{dep} deposited in a region with mass M and temperature T would give an increase in entropy-per-mass [49]

$$\Delta s \approx \frac{E_{\text{dep}}}{TM/m_u}, \quad (5.1)$$

where m_u is the atomic mass unit. As the entropy-per-baryon increases, nuclei (partially) melt and at least some of the photo-dissociation burden on the shock would be relieved, definitely helping the trigger of the explosion.

A comparison between the neutrino heating in the gain layer and the ALP one would be an interesting starting point to assess the impact of ALPs on the explosion. In particular, if the energy deposited by ALPs in the gain layer competes with the neutrino one before the explosion is artificially triggered ($t_{\text{pb}} \lesssim 250$ ms), the contribution of the decaying ALPs would help the revival of the shock.

At each time step, we evaluate the rate of energy deposited by neutrinos in the gain layer as

$$L_{\nu, \text{gain}}(t) = 4\pi \int_{R_{\text{gain}}}^{R_s} dr r^2 (Q_{\nu}^{+} - Q_{\nu}^{-}), \quad (5.2)$$

where Q_{ν}^{+} and Q_{ν}^{-} are respectively the heating and the cooling rate per unit volume, R_{gain} is the gain radius and R_s the shock radius, described in Sec. 2.4. By integrating the rate $L_{\nu, \text{gain}}$ over time, the energy deposition until the time t is obtained

$$E_{\nu, \text{dep}}(t) = \int_{t_0}^t d\tilde{t} L_{\nu, \text{gain}}(\tilde{t}). \quad (5.3)$$

where we fix $t_0 = 10$ ms since we are interested in the shock propagation after the neutronization burst. As shown in the upper panel of Fig. 15, the neutrino energy deposition rate is $L_{\nu, \text{gain}} \sim O(10^{51} - 10^{52} \text{ erg s}^{-1})$ for times $t_{\text{pb}} \lesssim 0.2$ s. The bump at $t_{\text{pb}} \approx 220$ ms corresponds to the artificial enhancement of the neutrino luminosity to trigger the explosion, while after the explosion has set up, $L_{\nu, \text{gain}}$ starts to decrease, becoming smaller than $O(10^{50} \text{ erg s}^{-1})$ at $t_{\text{pb}} = 1$ s. This implies that the energy deposited by neutrinos in the gain layer increases until $t_{\text{pb}} \approx 0.3$ s, saturating at $E_{\text{dep}} \approx 5 \times 10^{51} \text{ erg s}^{-1}$ for larger times, as shown in the lower panel of Fig. 15.

In order to evaluate the ALP heating, we focus our attention on the mass range $100 \text{ MeV} \leq m_a \leq 300 \text{ MeV}$, where the dominant processes are the production via photon coalescence and the absorption via decay. At each time step, we evaluate the axion luminosity through Eq. (3.7). Assuming for the sake of simplicity that ALPs are produced at a mean radius R_p evaluated in Eq. (4.15), the rate of energy deposited at a distance R results to be

$$L_{a, \text{dep}}(t, R) = L_a(t) \left[1 - \exp \left(- \int_{R_p}^R \frac{dr}{\lambda_{a \rightarrow \gamma\gamma}(\langle E_a \rangle, r)} \right) \right], \quad (5.4)$$

with $\lambda_{a \rightarrow \gamma\gamma}$ given by Eq. (4.8) and $\langle E_a \rangle$ the average axion energy over the emission spectrum. The rate at which the ALP energy is deposited in the gain layer results to be

$$L_{a, \text{gain}}(t) = L_{a, \text{dep}}(t, R_s) - L_{a, \text{dep}}(t, R_{\text{gain}}), \quad (5.5)$$

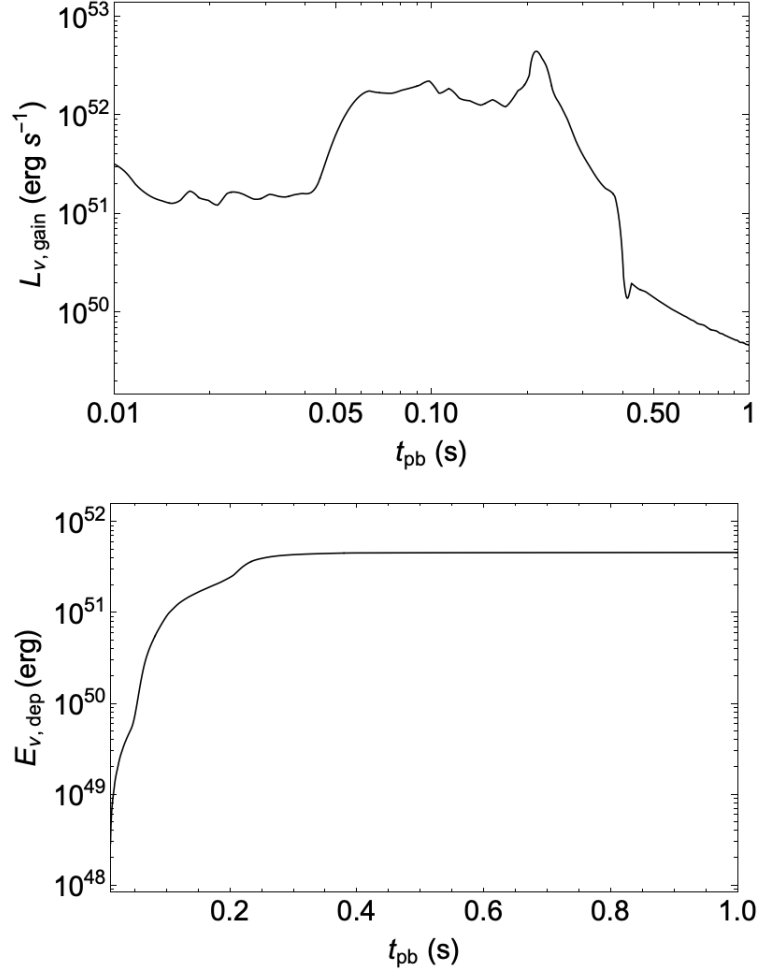


Figure 15. *Upper panel:* The neutrino energy deposition rate in the gain layer in the time-window $t_{\text{pb}} \in [10^{-2}, 1]$ s. *Lower Panel:* The energy deposited by neutrinos in the gain layer in the time-window $t_{\text{pb}} \in [10^{-2}, 1]$ s.

and the deposited energy is obtained by integrating over time

$$E_{a, \text{dep}} = \int_{t_0}^t d\tilde{t} L_{a, \text{gain}}(\tilde{t}) . \quad (5.6)$$

In Fig. 16 we show the contour plot in the $g_{a\gamma} - m_a$ plane of the ALP energy deposition rate in the gain layer at different post-bounce times. At $t_{\text{pb}} = 0.1$ s (upper panel) the ALP energy deposition rate results to be $L_{a, \text{gain}} \sim O(10^{50} \text{ erg s}^{-1})$, two orders of magnitude smaller than the neutrino contribution at the same time. At $t_{\text{pb}} = 0.2$ s (middle panel) the ALP energy deposition rate in the gain layer is not negligible with respect to the neutrino one $L_{\nu, \text{gain}} \approx 2.3 \times 10^{52} \text{ erg s}^{-1}$ (the dashed black contour in the middle panel of Fig. 16 corresponds to one tenth of $L_{\nu, \text{gain}}$). Therefore, ALPs could help the trigger of the explosion for a range of parameters not excluded by the energy-loss argument, namely in the mass range $150 \text{ MeV} \lesssim m_a \lesssim 220 \text{ MeV}$ and for values of the coupling constant $g_{a\gamma} \gtrsim 4 \times 10^{-10} \text{ GeV}^{-1}$. After the explosion is triggered, the axion heating rate continues to increase and becomes

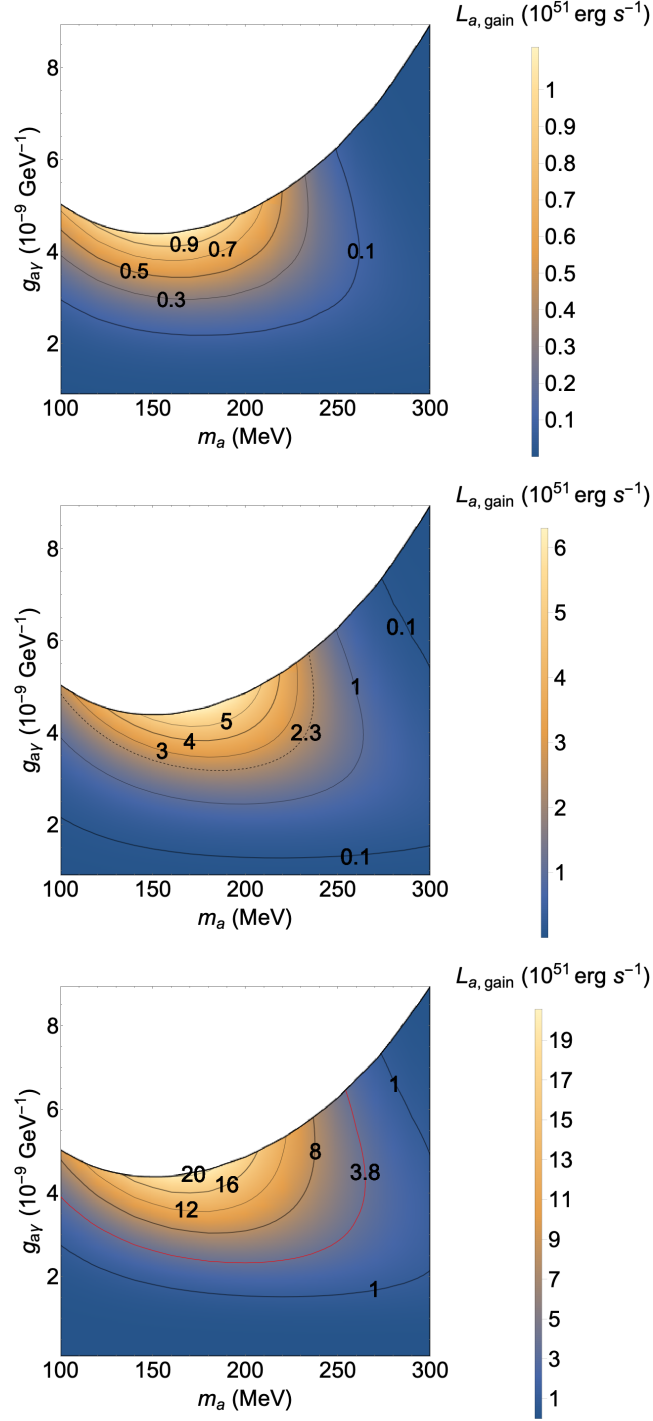


Figure 16. Isocontours in the $g_{a\gamma} - m_a$ plane of the ALP energy deposition rate in the gain layer at $t_{\text{pb}} = 0.1$ s (upper panel), $t_{\text{pb}} = 0.2$ s (middle panel), $t_{\text{pb}} = 0.3$ s (lower panel). The dashed contour in the middle panel corresponds to the one tenth of $L_{\nu,\text{gain}}$ at $t_{\text{pb}} = 0.2$ s, while the red contour in the lower panel corresponds to $L_{\nu,\text{gain}} \approx 3.8 \times 10^{51}$ erg s $^{-1}$ at $t_{\text{pb}} = 0.3$ s. In all the panels, the white region is excluded by the energy-loss argument.

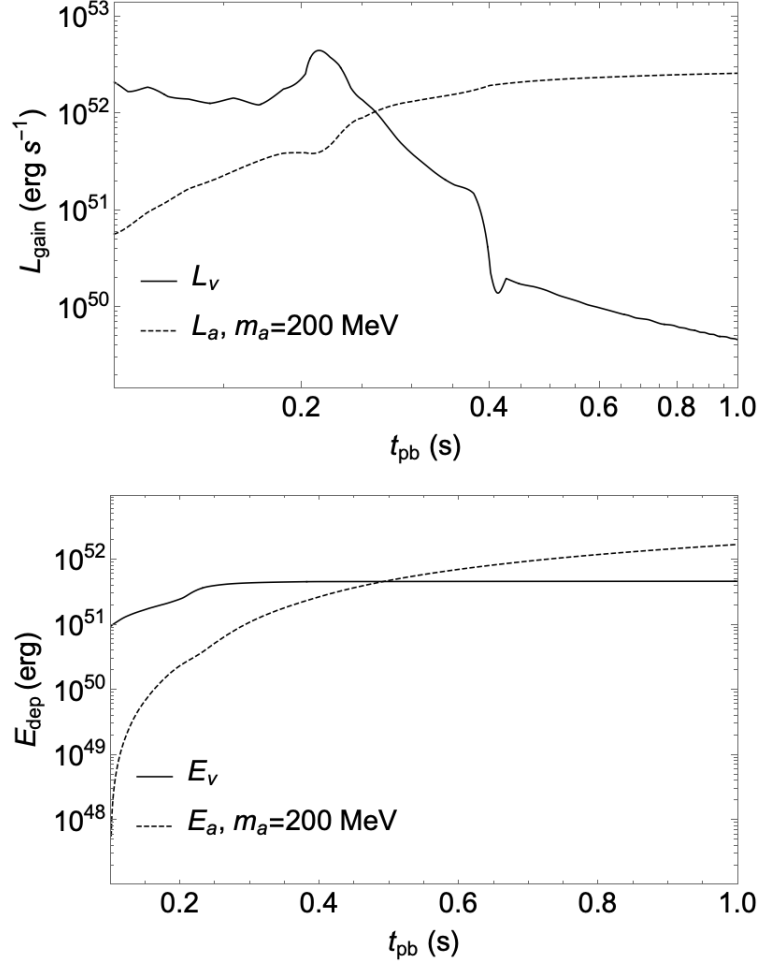


Figure 17. The time evolution of the energy deposition rate (upper panel) and of the energy deposited (lower panel) in the gain layer by neutrinos (continuous black curves) and by ALPs (dashed black curves) with mass $m_a = 200$ MeV and coupling constant $g_{a\gamma} = 4 \times 10^{-10} \text{ GeV}^{-1}$.

much larger than the neutrino one since this latter rapidly decreases. In particular, at $t_{\text{pb}} = 0.3$ s (lower panel) $L_{\nu, \text{gain}} \approx 4 \times 10^{51} \text{ erg s}^{-1}$, while $L_{a, \text{gain}} \sim O(10^{52} \text{ erg s}^{-1})$.

In Fig. 17 we show the time evolution of the energy deposition rate (upper panel) and of the energy deposited by ALPs in the gain layer (lower panel) for a fixed value of the coupling constant $g_{a\gamma} = 4 \times 10^{-10} \text{ GeV}^{-1}$ and a representative value of the axion mass $m_a = 200$ MeV (dashed black curves). At early times ($t_{\text{pb}} < 0.2$ s) $L_{a, \text{gain}} \ll L_{\nu, \text{gain}}$, while the ALP energy deposition rate becomes larger than $L_{\nu, \text{gain}}$ at times $t_{\text{pb}} \gtrsim 0.25$ s. Similarly, the energy deposited by ALPs in the gain layer is negligible at times $t_{\text{pb}} \lesssim 0.2$ s since it is more than an order of magnitude smaller than the one deposited by neutrinos at the same time. However, the former constantly increases and becomes greater than $5 \times 10^{51} \text{ erg}$ (the saturation value of the deposited neutrino energy) at times $t_{\text{pb}} \gtrsim 0.5$ s.

In particular, at $t_{\text{pb}} \approx 0.3$ s, $E_{a, \text{dep}} \sim O(10^{51} \text{ erg})$, the mass of the gain layer is $M \sim O(0.1 M_\odot)$ and the temperature in this region is $T \approx 2$ MeV. Therefore, by Eq. (5.1) one has $\Delta s \approx$ a few units of Boltzmann’s constant per baryon, an increase sufficient to partially melt nuclei and help the SN explosion.

One may conclude that for axion couplings below the energy-loss bound, one can still have a non negligible axion heating for the ALP parameters $150 \text{ MeV} \lesssim m_a \lesssim 220 \text{ MeV}$ and $g_{a\gamma} \gtrsim 4 \times 10^{-10} \text{ GeV}^{-1}$, which would help the SN explosion. In principle, one could convert the ALP deposited energy into an explosion energy E_{expl} [29] and constrain the ALP parameter space by imposing $E_{\text{expl}} \lesssim 3 \times 10^{51} \text{ erg}$ [50]. However, only a simulation including ALPs could provide reliable results and strengthen the validity of the hints obtained (see e.g. [51] for radiatively decaying standard axions or [52] for decaying sterile neutrinos).

6 Conclusions

In this work we used the state-of-the-art SN one-dimensional simulations to revise and update the mechanism of the emission from the SN core of heavy axion-like particles (ALPs), with masses of the order 1-100 MeV interacting with photons. In particular, we added the contribution of the photon coalescence process, neglected in previous studies, which dominates at masses $m_a \gtrsim 100 \text{ MeV}$ and allows to improve the previous constraints on the ALP parameter space. By combining the energy-loss argument in the free-streaming regime and the energy-transfer argument in the trapping regime, we confirm the previous bounds in the low-mass limit [$m_a \lesssim O(1 \text{ MeV})$] since the photon coalescence contribution is suppressed as m_a^4 , while constraints are sensitively improved at large masses. The inclusion of the photon coalescence allows to strengthen the previous bounds in the free-streaming regime by over an order of magnitude for masses $m_a \gtrsim 200 \text{ MeV}$.

The detailed analysis of the SN simulations, through which the time evolution of the characteristic radii of the SN atmosphere is obtained, allows to consistently apply an innovative method (which we dub the “modified luminosity criterion”) to explore the ALP parameter space, firstly proposed in [45] and based on the assumption that only the energy which cannot be efficiently reprocessed as neutrino one is relevant to constraint the ALP parameters. The two strategies give the same result in the case of free streaming ALPs, while they differ in the trapping regime, confirming the greater difficulties to deal with trapped ALPs.

In particular, the modified luminosity criterion allows to exclude larger values of the coupling constant $g_{a\gamma} \lesssim O(10^{-5} \text{ GeV}^{-1})$ in the low-mass limit ($m_a \lesssim 10 \text{ MeV}$), while at larger masses the bound is relaxed. In Fig. 18 we show the updated constraints on heavy ALPs. To be conservative, the purple area labelled “SN 1987A” is the region simultaneously excluded by both criteria discussed in this work.

The early time evolution of the SN simulation allows to assess the possible impact of the ALP production to trigger the SN explosion. In particular, following an original approach through which the neutrino heating rates and the ALP ones are compared, we endow a region of the parameter space with masses $m_a \approx 200 \text{ MeV}$ and coupling constant $g_{a\gamma} \gtrsim 4 \times 10^{-9} \text{ GeV}^{-1}$ for which the ALPs decaying into photons would provide an efficient energy deposition behind the shock which could help the SN explosion. It is quite intriguing that ALPs could be identified as the yet-missing piece of the puzzle to boost the supernova explosion energy in present neutrino-driven explosion models. A further exploration of this aspect motivates the involvement of multi-dimensional supernova models.

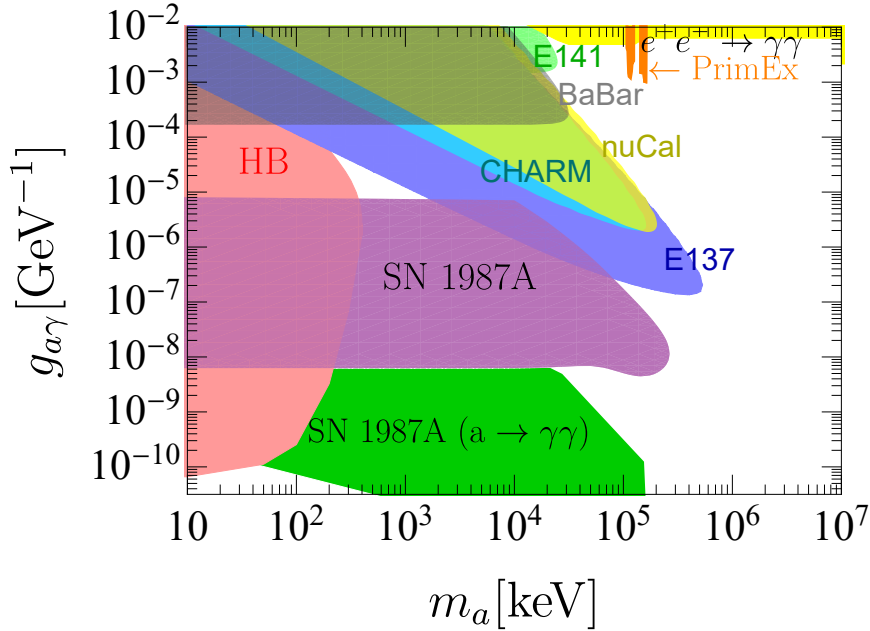


Figure 18. Overview of the heavy ALP parameter space in the plane $g_{a\gamma}$ vs m_a . The purple-filled region labelled “SN 1987A” represents our new exclusion result. The HB bound [12], the constraint from visible decays of ALPs produced in SN 1987A [21] and the experimental limits, compiled from Refs. [8, 12, 14], are also shown.

Acknowledgments

The work of P.C. and A.M. is partially supported by the Italian Istituto Nazionale di Fisica Nucleare (INFN) through the “Theoretical Astroparticle Physics” project and by the research grant number 2017W4HA7S “NAT-NET: Neutrino and Astroparticle Theory Network” under the program PRIN 2017 funded by the Italian Ministero dell’Università e della Ricerca (MUR). T. F. acknowledges support from the Polish National Science Center (NCN) under Grant No. 2016/23/B/ST2/00720 and No. 2019/33/B/ST9/03059. The supernova simulations are performed at the Wrocław Center for Scientific Computing and Networking (WCSS) in Wrocław (Poland).

References

- [1] L. Di Luzio, M. Giannotti, E. Nardi and L. Visinelli, “The landscape of QCD axion models,” [arXiv:2003.01100 [hep-ph]].
- [2] P. Svrcek and E. Witten, “Axions In String Theory,” JHEP **0606**, 051 (2006) doi:10.1088/1126-6708/2006/06/051 [hep-th/0605206].
- [3] A. Arvanitaki, S. Dimopoulos, S. Dubovsky, N. Kaloper and J. March-Russell, “String Axiverse,” Phys. Rev. D **81**, 123530 (2010) doi:10.1103/PhysRevD.81.123530 [arXiv:0905.4720 [hep-th]].
- [4] M. Cicoli, M. Goodsell and A. Ringwald, “The type IIB string axiverse and its low-energy

- phenomenology,” JHEP **1210**, 146 (2012) doi:10.1007/JHEP10(2012)146 [arXiv:1206.0819 [hep-th]].
- [5] P. W. Graham, D. E. Kaplan and S. Rajendran, “Cosmological Relaxation of the Electroweak Scale,” Phys. Rev. Lett. **115**, no. 22, 221801 (2015) doi:10.1103/PhysRevLett.115.221801 [arXiv:1504.07551 [hep-ph]].
 - [6] Y. Hochberg, E. Kuflik, R. McGehee, H. Murayama and K. Schutz, “Strongly interacting massive particles through the axion portal,” Phys. Rev. D **98**, no. 11, 115031 (2018) doi:10.1103/PhysRevD.98.115031 [arXiv:1806.10139 [hep-ph]].
 - [7] C. Boehm, M. J. Dolan, C. McCabe, M. Spannowsky and C. J. Wallace, JCAP **1405**, 009 (2014) doi:10.1088/1475-7516/2014/05/009 [arXiv:1401.6458 [hep-ph]].
 - [8] M. J. Dolan, T. Ferber, C. Hearty, F. Kahlhoefer and K. Schmidt-Hoberg, “Revised constraints and Belle II sensitivity for visible and invisible axion-like particles,” JHEP **1712**, 094 (2017) doi:10.1007/JHEP12(2017)094 [arXiv:1709.00009 [hep-ph]].
 - [9] D. Cadamuro, S. Hannestad, G. Raffelt and J. Redondo, “Cosmological bounds on sub-MeV mass axions,” JCAP **1102**, 003 (2011) doi:10.1088/1475-7516/2011/02/003 [arXiv:1011.3694 [hep-ph]].
 - [10] D. Cadamuro and J. Redondo, “Cosmological bounds on pseudo Nambu-Goldstone bosons,” JCAP **1202**, 032 (2012) doi:10.1088/1475-7516/2012/02/032 [arXiv:1110.2895 [hep-ph]].
 - [11] P. F. Depta, M. Hufnagel and K. Schmidt-Hoberg, “Robust cosmological constraints on axion-like particles,” arXiv:2002.08370 [hep-ph].
 - [12] P. Carena, O. Straniero, B. Döbrich, M. Giannotti, G. Lucente and A. Mirizzi, “Constraints on the coupling with photons of heavy axion-like-particles from Globular Clusters,” [arXiv:2004.08399 [hep-ph]].
 - [13] J. Jaeckel and M. Spannowsky, “Probing MeV to 90 GeV axion-like particles with LEP and LHC,” Phys. Lett. B **753**, 482 (2016) doi:10.1016/j.physletb.2015.12.037 [arXiv:1509.00476 [hep-ph]].
 - [14] B. Döbrich, J. Jaeckel and T. Spadaro, “Light in the beam dump. Axion-Like Particle production from decay photons in proton beam-dumps,” JHEP **1905**, 213 (2019) doi:10.1007/JHEP05(2019)213 [arXiv:1904.02091 [hep-ph]].
 - [15] J. W. Brockway, E. D. Carlson and G. G. Raffelt, “SN1987A gamma-ray limits on the conversion of pseudoscalars,” Phys. Lett. B **383**, 439-443 (1996) doi:10.1016/0370-2693(96)00778-2 [arXiv:astro-ph/9605197 [astro-ph]].
 - [16] J. Grifols, E. Masso and R. Toldra, “Gamma-rays from SN1987A due to pseudoscalar conversion,” Phys. Rev. Lett. **77**, 2372-2375 (1996) doi:10.1103/PhysRevLett.77.2372 [arXiv:astro-ph/9606028 [astro-ph]].
 - [17] A. Payez, C. Evoli, T. Fischer, M. Giannotti, A. Mirizzi and A. Ringwald, “Revisiting the SN1987A gamma-ray limit on ultralight axion-like particles,” JCAP **02**, 006 (2015) doi:10.1088/1475-7516/2015/02/006 [arXiv:1410.3747 [astro-ph.HE]].
 - [18] E. Masso and R. Toldra, “On a light spinless particle coupled to photons,” Phys. Rev. D **52**, 1755-1763 (1995) doi:10.1103/PhysRevD.52.1755 [arXiv:hep-ph/9503293 [hep-ph]].
 - [19] J. S. Lee, “Revisiting Supernova 1987A Limits on Axion-Like-Particles,” [arXiv:1808.10136 [hep-ph]].
 - [20] M. Giannotti, L. Duffy and R. Nita, “New constraints for heavy axion-like particles from supernovae,” JCAP **01**, 015 (2011) doi:10.1088/1475-7516/2011/01/015 [arXiv:1009.5714 [astro-ph.HE]].

- [21] J. Jaeckel, P. Malta and J. Redondo, “Decay photons from the axionlike particles burst of type II supernovae,” *Phys. Rev. D* **98**, no.5, 055032 (2018) doi:10.1103/PhysRevD.98.055032 [arXiv:1702.02964 [hep-ph]].
- [22] A. Mezzacappa and S. W. Bruenn, “A numerical method for solving the neutrino Boltzmann equation coupled to spherically symmetric stellar core collapse,” *Astrophys. J.* **405**, 669 (1993). doi:10.1086/172395
- [23] M. Liebendoerfer, O. E. B. Messer, A. Mezzacappa, S. W. Bruenn, C. Y. Cardall and F. K. Thielemann, “A Finite difference representation of neutrino radiation hydrodynamics for spherically symmetric general relativistic supernova simulations,” *Astrophys. J. Suppl.* **150**, 263 (2004) doi:10.1086/380191 [astro-ph/0207036].
- [24] T. Fischer, G. Guo, A. A. Dzhioev, G. Martinez-Pinedo, M. R. Wu, A. Lohs and Y. Z. Qian, “Neutrino signal from proto-neutron star evolution: Effects of opacities from charged-current neutrino interactions and inverse neutron decay,” *Phys. Rev. C* **101**, no.2, 025804 (2020) doi:10.1103/PhysRevC.101.025804 [arXiv:1804.10890 [astro-ph.HE]].
- [25] S. E. Woosley, A. Heger and T. A. Weaver, “The evolution and explosion of massive stars”, *Rev. Mod. Phys.* **74**, 1015 (2002) doi:10.1103/RevModPhys.74.1015
- [26] K. Nomoto “Evolution of 8-10 solar mass stars toward electron capture supernovae. I - Formation of electron-degenerate O + NE + MG cores.” *Astrophys. J.* **277**, 791 (1984) doi:10.1086/161749
- [27] S. Jones, R. Hirschi, K. Nomoto, et al. “Advanced Burning Stages and Fate of 8-10 M_{\odot} Stars,” *Astrophys. J.* **772**, 150 (2013) doi:10.1088/0004-637X/772/2/150
- [28] L. Hudepohl, B. Muller, H. T. Janka, A. Marek and G. Raffelt, “Neutrino Signal of Electron-Capture Supernovae from Core Collapse to Cooling,” *Phys. Rev. Lett.* **104**, 251101 (2010) doi:10.1103/PhysRevLett.104.251101 [arXiv:0912.0260 [astro-ph.SR]].
- [29] T. Fischer, S. Whitehouse, A. Mezzacappa, F. K. Thielemann and M. Liebendorfer, “Protoneutron star evolution and the neutrino driven wind in general relativistic neutrino radiation hydrodynamics simulations,” *Astron. Astrophys.* **517**, A80 (2010) doi:10.1051/0004-6361/200913106 [arXiv:0908.1871 [astro-ph.HE]].
- [30] M. Hempel and J. Schaffner-Bielich, “Statistical Model for a Complete Supernova Equation of State,” *Nucl. Phys. A* **837**, 210 (2010) doi:10.1016/j.nuclphysa.2010.02.010 [arXiv:0911.4073 [nucl-th]].
- [31] M. Hempel, T. Fischer, J. Schaffner-Bielich and M. Liebendorfer, “New Equations of State in Simulations of Core-Collapse Supernovae,” *Astrophys. J.* **748**, 70 (2012) doi:10.1088/0004-637X/748/1/70 [arXiv:1108.0848 [astro-ph.HE]].
- [32] M. Hempel, “Nucleon self-energies for supernova equations of state,” *Phys. Rev. C* **91**, 055807 (2015) doi:10.1103/PhysRevC.91.055807 [arXiv:1410.6337 [nucl-th]].
- [33] T. Fischer, M. Hempel, I. Sagert, Y. Suwa and J. Schaffner-Bielich, “Symmetry energy impact in simulations of core-collapse supernovae” *European Physical Journal* **A50**, 46 (2014) doi:10.1140/epja/i2014-14046-5
- [34] H. T. Janka, “Conditions for shock revival by neutrino heating in core collapse supernovae,” *Astron. Astrophys.* **368**, 527 (2001) doi:10.1051/0004-6361:20010012 [arXiv:astro-ph/0008432 [astro-ph]].
- [35] T. Fischer, “The role of medium modifications for neutrino-pair processes from nucleon-nucleon bremsstrahlung - Impact on the protoneutron star deleptonization,” *Astron. Astrophys.* **593**, A103 (2016) doi:10.1051/0004-6361/201628991 [arXiv:1608.05004 [astro-ph.HE]].
- [36] T. Fischer, G. Martínez-Pinedo, M. Hempel, and M. Liebendörfer, “Neutrino spectra evolution

- during protoneutron star deleptonization,” *Phys. Rev.* **D85**, 083003 (2012)
doi:10.1103/PhysRevD.85.083003
- [37] G. Raffelt and L. Stodolsky, “Mixing of the Photon with Low Mass Particles,” *Phys. Rev. D* **37**, 1237 (1988) doi:10.1103/PhysRevD.37.1237
 - [38] L. Di Lella, A. Pilaftsis, G. Raffelt and K. Zioutas, “Search for solar Kaluza-Klein axions in theories of low scale quantum gravity,” *Phys. Rev. D* **62**, 125011 (2000)
doi:10.1103/PhysRevD.62.125011 [arXiv:hep-ph/0006327 [hep-ph]].
 - [39] A. Kopf and G. Raffelt, “Photon dispersion in a supernova core,” *Phys. Rev. D* **57** (1998) 3235
doi:10.1103/PhysRevD.57.3235 [astro-ph/9711196].
 - [40] G. Pagliaroli, F. Vissani, M. Costantini and A. Ianni, “Improved analysis of SN1987A antineutrino events,” *Astropart. Phys.* **31**, 163-176 (2009)
doi:10.1016/j.astropartphys.2008.12.010 [arXiv:0810.0466 [astro-ph]].
 - [41] G. G. Raffelt, “Astrophysical axion bounds,” *Lect. Notes Phys.* **741**, 51-71 (2008)
doi:10.1007/978-3-540-73518-2_3 [arXiv:hep-ph/0611350 [hep-ph]].
 - [42] H. Dreiner, C. Hanhart, U. Langenfeld and D. R. Phillips, “Supernovae and light neutralinos: SN1987A bounds on supersymmetry revisited,” *Phys. Rev. D* **68**, 055004 (2003)
doi:10.1103/PhysRevD.68.055004 [arXiv:hep-ph/0304289 [hep-ph]].
 - [43] G. G. Raffelt, “Stars as laboratories for fundamental physics : The astrophysics of neutrinos, axions, and other weakly interacting particles,” Chicago, USA: Univ. Pr. (1996) 664 p.
 - [44] G. Raffelt and D. Seckel, “Bounds on Exotic Particle Interactions from SN 1987a,” *Phys. Rev. Lett.* **60**, 1793 (1988) doi:10.1103/PhysRevLett.60.1793
 - [45] J. H. Chang, R. Essig and S. D. McDermott, “Revisiting Supernova 1987A Constraints on Dark Photons,” *JHEP* **01**, 107 (2017) doi:10.1007/JHEP01(2017)107 [arXiv:1611.03864 [hep-ph]].
 - [46] F. Ertas and F. Kahlhoefer, “On the interplay between astrophysical and laboratory probes of MeV-scale axion-like particles,” [arXiv:2004.01193 [hep-ph]].
 - [47] W. DeRocco and P. W. Graham, “Constraining Primordial Black Hole Abundance with the Galactic 511 keV Line,” *Phys. Rev. Lett.* **123**, no.25, 251102 (2019)
doi:10.1103/PhysRevLett.123.251102 [arXiv:1906.07740 [astro-ph.CO]].
 - [48] B. Mller, T. Melson, A. Heger and H. T. Janka, “Supernova simulations from a 3D progenitor model Impact of perturbations and evolution of explosion properties,” *Mon. Not. Roy. Astron. Soc.* **472**, no.1, 491-513 (2017) doi:10.1093/mnras/stx1962 [arXiv:1705.00620 [astro-ph.SR]].
 - [49] G. M. Fuller, A. Kusenko and K. Petraki, “Heavy sterile neutrinos and supernova explosions,” *Phys. Lett. B* **670**, 281-284 (2009) doi:10.1016/j.physletb.2008.11.016 [arXiv:0806.4273 [astro-ph]].
 - [50] A. Sung, H. Tu and M. R. Wu, “New constraint from supernova explosions on light particles beyond the Standard Model,” *Phys. Rev. D* **99**, no.12, 121305 (2019)
doi:10.1103/PhysRevD.99.121305 [arXiv:1903.07923 [hep-ph]].
 - [51] D. N. Schramm and J. R. Wilson, “SUPERNOVAE INDUCED BY AXION LIKE PARTICLES,” *Astrophys. J.* **260**, 868 (1982) doi:10.1086/160305
 - [52] T. Rembiasz, M. Obergaulinger, M. Masip, M. . Prez-Garca, M. . Aloy and C. Albertus, “Heavy sterile neutrinos in stellar core-collapse,” *Phys. Rev. D* **98**, no.10, 103010 (2018)
doi:10.1103/PhysRevD.98.103010 [arXiv:1806.03300 [astro-ph.HE]].